High-pressure granulite-facies metamorphism in central Dronning Maud Land (East Antarctica): implications for Gondwana assembly

Elsevier Editorial System(tm) for Lithos
Manuscript Draft

Manuscript Number:

Title: High-pressure granulite-facies metamorphism in central Dronning Maud Land (Antarctica): implications for Gondwana assembly

Article Type: Regular Article

Keywords: Antarctica; Grenvillian orogeny; Pan-African orogeny; Gondwana; mafic/ultramafic rocks; HP-HT granulite

Corresponding Author: Dr. rosaria Palmeri, PhD

Corresponding Author's Institution: Siena University

First Author: rosaria Palmeri, PhD

Order of Authors: rosaria Palmeri, PhD; Gaston Godard; Gianfranco Di Vincenzo; Sonia Sandroni; Franco Talarico

Abstract: The Dronning Maud Land (DML; East Antarctica) is a key region for the study of the Grenvillian (1.3-0.9 Ga) and Pan-African (0.6-0.5 Ga) orogenies, which have led to the assembly of Rodinia and Gondwana supercontinents respectively. Central DML is characterized by a Pan-African tectono-metamorphic evolution that involved Mesoproterozoic protoliths related to the Grenville orogenic cycle. The Conradgebirge area, one of the best rock exposures of central DML, consists of orthogneisses, derived from both volcanic and plutonic protoliths, and minor metasediments, intruded by Cambrian syn- to post-metamorphic plutons and dykes.
Mafic-ultramafic boudins in the metavolcanic and metaplutonic gneisses from Conradgebirge consist of amphibolites and high-grade Grt-bearing pyroxene- and amphibole-rich fels. They occur either as discontinuous levels or as pods boudinaged within highly-strained and strongly-migmatized gneisses. Bulk-rock major and trace-element compositions suggest derivation from E-MORB to OIB protoliths for the mafic rocks boudinaged in metaplutonic gneisses, whereas a calc-alkaline signature is common for the mafic boudins in metavolcanic rocks. Most of the magmatic protoliths of the mafic as well as felsic rocks likely formed at the Mesoproterozoic during the Grenville orogenic cycle, in an arc/back-arc environment.
The microstructural study and P-T modelling of an ultramafic metagabbroic rock reveal a prograde metamorphic evolution from amphibolite-facies (ca. 0.5 GPa; 500°C) up to high-P granulite-facies conditions (ca. 1.5-1.7 GPa; 960-970°C). Partial melting is testified by nanogranitoid inclusions enclosed in garnet. An almost isothermal decompression down to ca. 0.4 GPa and 750-850°C produced well-developed An+Opx-bearing symplectites around garnet. The final isobaric cooling took place at ~505-480 Ma, as revealed by 40Ar-39Ar dating of amphibole and biotite.
The above reconstruction traces a clockwise P-T evolution with a peak metamorphism at high-P granulite-facies conditions, whose age is uncertain but possibly occurred at nearly 570 Ma, followed by a decompression promoted by a transpressive regime before the collapse of the orogeny structures at nearly 500 Ma. This tectono-metamorphic scenario seems representative of the evolution resulting from the Pan-

African collision between the East-Gondwana and West-Gondwana blocks that led to the final assembly of Gondwana and, in DML, to the formation of the Mozambique Belt extension into Antarctica.

Cover letter

Siena, September 4st 2017

Dear Editor,

Here is the paper "**High-pressure granulite-facies metamorphism in central Dronning Maud Land (Antarctica): implications for Gondwana assembly**" by Rosaria Palmeri, Gaston Godard, Gianfranco Di Vincenzo, Sonia Sandroni and Franco Talarico for submission to Lithos. We hope that the petrological and geochemical results reported here are suitable for your journal and interesting for the researchers involved into the evolution of the Pan-African orogen, in Antarctica and elsewhere.

The paper has not been published before. A companion paper dealing about the presence of partial melt within garnet in one of the rocks studied here is already submitted to The American Mineralogist ("**Partial melting of ultramafic granulites from Dronning Maud Land, Antarctica: constraints from melt inclusions and thermodynamic modeling**" by S. Ferrero, G. Godard, R. Palmeri, B. Wunder, B. Cesare).

The content has been approved by all co-authors.

We propose as reviewers two specialists of the central Dronning Maud Land (J. Jacobs; W. Bauer), and two petrologists, expert of East Antarctica (R.P. Ménot; Martin Hand):

Joachim Jacobs, Department of Earth Science, University of Bergen, Allegaten 41, 5007 Bergen, Norway.
joachim.jacobs@geo.uib.no

Wilfried Bauer, School of Geosciences, Energy and Mineral Resources, WüllnerStr. 2, 52062 Aachen, Germany.
bauer@geol.rwth-aachen.de

René-Pierre Ménot, Université Jean Monnet, Saint-Étienne, UMR CNRS IRD 6524, Laboratoire Magmas et Volcans, F-42023 Saint-Étienne, France.
rene.pierre.menot@univ-st-etienne.fr

Martin Hand, Department of Earth Science, University of Adelaide, Adelaide South Australia, 5005 Australia.
martin.hand@adelaide.edu.au

Best regards,

Rosaria Palmeri

The Dronning Maud Land (DML; East Antarctica) is a key region for the study of the Grenvillian (1.3–0.9 Ga) and Pan-African (0.6–0.5 Ga) orogenies, which have led to the assembly of Rodinia and Gondwana supercontinents respectively. Central DML is characterized by a Pan-African tectono-metamorphic evolution that involved Mesoproterozoic protoliths related to the Grenville orogenic cycle. The Conradgebirge area, one of the best rock exposures of central DML, consists of orthogneisses, derived from both volcanic and plutonic protoliths, and minor metasediments, intruded by Cambrian syn- to post-metamorphic plutons and dykes.

Mafic-ultramafic boudins in the metavolcanic and metaplutonic gneisses from Conradgebirge consist of amphibolites and high-grade Grt-bearing pyroxene- and amphibole-rich fels. They occur either as discontinuous levels or as pods boudinaged within highly-strained and strongly-migmatized gneisses. Bulk-rock major and trace-element compositions suggest derivation from E-MORB to OIB protoliths for the mafic rocks boudinaged in metaplutonic gneisses, whereas a calc-alkaline signature is common for the mafic boudins in metavolcanic rocks. Most of the magmatic protoliths of the mafic as well as felsic rocks likely formed at the Mesoproterozoic during the Grenville orogenic cycle, in an arc/back-arc environment.

The microstructural study and *P*–*T* modelling of an ultramafic metagabbroic rock reveal a prograde metamorphic evolution from amphibolite-facies (ca. 0.5 GPa; 500°C) up to high-*P* granulite-facies conditions (ca. 1.5–1.7 GPa; 960–970°C). Partial melting is testified by nanogranitoid inclusions enclosed in garnet. An almost isothermal decompression down to ca. 0.4 GPa and 750–850°C produced well-developed An+Opx-bearing symplectites around garnet. The final isobaric cooling took place at ~505–480 Ma, as revealed by ^{40}Ar-^{39}Ar dating of amphibole and biotite.

The above reconstruction traces a clockwise *P-T* evolution with a peak metamorphism at high-*P* granulite-facies conditions, whose age is uncertain but possibly occurred at nearly 570 Ma, followed by a decompression promoted by a transpressive regime before the collapse of the orogeny structures at nearly 500 Ma. This tectono-metamorphic scenario seems representative of the evolution resulting from the Pan-African collision between the East-Gondwana and West-Gondwana blocks that led to the final assembly of Gondwana and, in DML, to the formation of the Mozambique Belt extension into Antarctica.

***Highlights (for review)**

Highlights

(Ultra)mafic rocks of East Antarctica were metamorphosed during the Gondwana assembly

Their magmatic protoliths are related to the Mesoproteroic Grenville orogenic cycle

High-*P* metamorphism (up to 1.5–1.7 GPa, 960–970°C) produced melt preserved in garnet

Isothermal exhumation developed An+Opx symplectites before cooling at 505–480 Ma

They are related to the Pan-African Mozambique belt extension into Antarctica

,

High-pressure granulite-facies metamorphism in central Dronning Maud Land (Antarctica): implications for Gondwana assembly

Rosaria Palmeri[a,*], Gaston Godard[b], Gianfranco Di Vincenzo[c], Sonia Sandroni[a], Franco M. Talarico[a,d]

[a] Museo Nazionale dell'Antartide, Università degli Studi di Siena, via Laterina 8, 53100 Siena, Italy
[b] Institut de Physique du Globe, Université Paris Diderot, UMR 7154 CNRS, F-75252 Paris, France.
[c] Istituto di Geoscienze e Georisorse, CNR, via Moruzzi 1, 56124 Pisa, Italy.
[d] Dipartimento di Scienze Fisiche, della Terra e dell'Ambiente, Università degli Studi di Siena, via Laterina 8, 53100 Siena, Italy.
* Corresponding author.
E-mail address: rosaria.palmeri@unisi.it (R. Palmeri).

Keywords: Antarctica, Grenvillian orogeny, Pan-African orogeny, Gondwana, mafic/ultramafic rocks, HP-HT granulite.

Abbreviations: Mineral and end-member abbreviations are from Kretz (1983), with the addition of Liq (silicate melt liquid), Opm (opaque mineral) and Sulph (sulphide); "ppm" is used for μg/g.

Abstract

The Dronning Maud Land (DML; East Antarctica) is a key region for the study of the Grenvillian (1.3–0.9 Ga) and Pan-African (0.6–0.5 Ga) orogenies, which have led to the assembly of Rodinia and Gondwana supercontinents respectively. Central DML is characterized by a Pan-African tectono-metamorphic evolution that involved Mesoproterozoic protoliths related to the Grenville orogenic cycle. The Conradgebirge area, one of the best rock exposures of central DML, consists of orthogneisses, derived from both volcanic and plutonic protoliths, and minor metasediments, intruded by Cambrian syn- to post-metamorphic plutons and dykes.

Mafic-ultramafic boudins in the metavolcanic and metaplutonic gneisses from Conradgebirge consist of amphibolites and high-grade Grt-bearing pyroxene- and amphibole-rich fels. They occur either as discontinuous levels or as pods boudinaged within highly-strained and strongly-migmatized gneisses. Bulk-rock major and trace-element compositions suggest derivation from E-MORB to OIB protoliths for the mafic rocks boudinaged in metaplutonic gneisses, whereas a calc-alkaline signature is common for the mafic boudins in metavolcanic rocks. Most of the magmatic protoliths of the mafic as well as felsic rocks likely formed at the Mesoproterozoic during the Grenville orogenic cycle, in an arc/back-arc environment.

The microstructural study and *P*–*T* modelling of an ultramafic metagabbroic rock reveal a prograde metamorphic evolution from amphibolite-facies (ca. 0.5 GPa; 500°C) up to high-*P* granulite-facies conditions (ca. 1.5–1.7 GPa; 960–970°C). Partial melting is testified by nanogranitoid inclusions enclosed in garnet. An almost isothermal decompression down to ca. 0.4 GPa and 750–850°C produced well-developed An+Opx-bearing symplectites around garnet. The final isobaric cooling took place at ~505–480 Ma, as revealed by ^{40}Ar-^{39}Ar dating of amphibole and biotite.

The above reconstruction traces a clockwise *P-T* evolution with a peak metamorphism at high-*P* granulite-facies conditions, whose age is uncertain but possibly occurred at nearly 570 Ma, followed by a decompression promoted by a transpressive regime before the collapse of the orogeny structures at nearly 500 Ma. This tectono-metamorphic scenario seems representative of the evolution resulting from the Pan-African collision between the East-Gondwana and West-Gondwana blocks that led to the final assembly of Gondwana and, in DML, to the formation of the Mozambique Belt extension into Antarctica.

1. Introduction

Granulite-facies rocks, reported in recent and – mostly – old orogenic belts, usually denote high-*T* (HT) metamorphic conditions during orogeny (Harley, 1989). Besides such HT granulites, high-*P* (HP) granulite-facies rocks have also been reported, more recently, in various orogenic belts (e.g. Baldwin et al., 2003;

Elvevold and Gilotti, 2000; Gayk et al., 1995; O'Brien and Rözler, 2003; Pauly et al., 2016; Rözler and Romer, 2001; Zhao et al., 2001). HP granulites can form along relatively high dP/dT gradients typical of subduction processes and can reach *P-T* conditions corresponding to mantle depths. They are typically found in the internal zones of orogenic belts, testifying major plate tectonic processes such as crustal thickening above subduction zones or stacking/doubling of the crust during continental collision (e.g. Harley, 1989; O'Brien and Rözler, 2003; Pauly et al., 2016).

East Antarctica provides many examples of granulite-facies metamorphism, including the well-known Archaean ultrahigh-*T* granulites from the Napier Complex (Enderby Land: Harley et al., 2013). Precambrian terranes were accreted onto Archaean nuclei in the course of several collisional orogenies, namely the Grenville (~1.0 Ga) and Pan-African (~600–500 Ma) orogens, leading to the assembly of, respectively, the Rodinia and Gondwana supercontinents (Fig. 1; Boger, 2011). High-grade metamorphic rocks have been ascribed to these orogens in East Antarctica, including a few eclogites (Schmädicke and Will, 2006) and – mostly – granulites (e.g., Black et al., 1987; Engvik and Elvevold, 2004; Engvik et al., 2007; Grew et al., 1988; Harley, 1985; Makimoto et al., 1990; Pauly et al., 2016; Shiraishi et al., 1997). However, as emphasized by Godard and Palmeri (2013) and Pauly et al. (2016), there is a lot of uncertainties in this region about the orogen to which these rocks should be ascribed (Grenvillian, Grenvillian reworked during Pan-African, or Pan-African), as well as about the reached metamorphic conditions (eclogite, HP-granulite or medium/low-*P*-granulite facies). In part, this is due to the petrographic convergence between retrograded eclogites and HP mafic granulites, the latter being characterized by Opx-free assemblages consisting of Grt+Cpx±Pl±Qtz±Cam (Pattison, 2003).

Here, we describe the petrological and geochemical features of selected granulite-facies mafic-ultramafic rocks from Conradgebirge in central Dronning Maud Land (DML), East Antarctica. A particular attention is given to a garnet-bearing ultramafic rock that preserved an HP-granulite-facies assemblage and whose garnet encloses "nanogranitoid" after melt inclusions – the first ever recorded in mafic rocks (Ferrero et al., 2016), and whose study is presented in detail elsewhere (Ferrero et al., 2017). The *P-T* evolution of the rock is modelled through *P-T* pseudosection calculations and its amphibole and biotite are dated by the ^{40}Ar-^{39}Ar technique. The results allow us to clarify the meaning of these HP-granulite-facies terranes in the context of the Pan-African orogeny that led to the Neoproterozoic assembly of the Gondwana supercontinent, and to discuss whether part of their evolution should be ascribed to the earlier Grenvillian orogeny.

2. Geological setting

The DML mountains extend from 18° W to 28° E, parallel to the coastline of Antarctica (Fig. 2). It is a key region for the palaeogeographic reconstructions of continents from the Mesoproterozoic to the Cambrian, as it potentially contains relevant geological records documenting the formation and dispersion of Rodinia and the subsequent assembly of Gondwana (Fig. 1; Bauer et al., 2003; Jacobs, 1999; Jacobs et al., 1998, 2003; Satish-Kumar et al., 2008). Palaeomagnetic (Gose et al., 1997), geochronological (Jacobs et al., 1998; Satish-Kumar et al., 2008, 2013) and aeromagnetic (Golynsky and Jacob, 2001) surveys show that DML can be subdivided into three zones with different geological histories (Bauer et al., 2003): a) an Archaean craton with an undeformed Proterozoic cover; b) a late Mesoproterozoic collision orogen related to the amalgamation of the Neoproterozoic supercontinent Rodinia; c) a Pan-African collision belt that led to the Gondwana assembly, with pre-Pan-African relicts and voluminous syn- to post-tectonic intrusive rocks. The latter is mainly exposed in central DML, which is regarded, in many Gondwana reconstructions (Fig. 1), as the southern extension of the Mozambique belt into East Antarctica (Jacobs et al., 1998). The Mozambique belt is one of the most extensive orogens in the Earth's history (Holmes, 1951); it is interpreted as having formed during the closure of the Mozambique Ocean and the subsequent collision and amalgamation of East and West Gondwana during Pan-African orogeny (Bauer et al., 2003; Elvevold and Engvik, 2013; Grunow et al., 1996; Hoffman, 1991; Jacobs, 1999; Jacobs et al., 1998; Pauly et al., 2016; Shackleton, 1996).

Several major lithological units have been distinguished and mapped in the metamorphic basement of central DML (Paech et al., 2004). They include metaigneous and metasedimentary units, as well as syn- to post-metamorphic plutons and dykes (Fig. 2). According to Jacobs (1999) and Bauer et al. (2003, 2004), the oldest formation consists of a thick supracrustal pile made of banded felsic and mafic gneisses interpreted as a bimodal volcanic sequence (U-Pb age on zircon 1130 ± 12 Ma: Jacobs, 1999; Jacobs et al., 1998), interlayered with sedimentary rocks. This volcanic complex was later intruded by a voluminous granitoid batholith and sheet-like felsic intrusions (U-Pb age on zircon 1083 ± 20 Ma: Jacobs, 1999; Jacobs et al., 1998). The two formations, intensely metamorphosed and deformed, were transformed into metavolcanic and metaplutonic complexes during the Pan-African orogenic cycle. Central DML was lately (600–510 Ma) intruded by two anorthosite suites and granites.

The earliest deformation structure (D_1) is evidenced by intrafolial isoclinal folds in paragneisses and metavolcanic rocks of the metavolcanic complex. It is assumed to be a Late Mesoproterozoic event, because of the metamorphic (M_1) age provided by zircons collected from a metavolcanic felsic gneiss (~1080 Ma: Bauer et al., 2003; Jacobs, 1999; Jacobs et al., 1998). The most prominent deformation phase (D_2) is responsible for major N-vergent folds with gently NE-to-E-plunging axes. It produced the main foliation, coeval with granulite-facies metamorphism (M_2) and syntectonic migmatization, whose age of ~570 Ma (Jacobs et al. 1998) relates the event to the Pan-African orogenic cycle. To the same orogenic cycle are attributed the later D_3 and D_4 events. D_3 is characterized by major sinistral shear zones (e.g. SOSZ in Fig. 2) and transpressive N-S trending folds, coeval with granulite- to amphibolite-facies metamorphism (M_3). Finally, D_4 is defined by discrete extensional shear zones associated with Cambrian intrusions of syenite and charnockite, and a retrograde amphibolite-facies metamorphism (M_4).

Conradgebirge, in Orvinfjella (Figs. 2 and 3), is one of the best exposures of central DML where the D_1 to D_4 tectono-metamorphic evolution can be followed (Colombo and Talarico, 2004). To the North, Cambrian syenite and charnockite intrude the metavolcanic complex, which consists here of amphibole-bearing gneisses, amphibolites and plagiogneisses with minor gabbros and ultramafic lenses (yellow in Fig. 3). This complex is interleaved with rare thin belts of metasedimentary rocks, mainly Bt+Sil+Grt±Opx gneisses, calc-silicate rocks, marbles and quartzites (blue in Fig. 3). In the central part of Conradgebirge, a metaplutonic complex made up of garnet-bearing migmatitic augen orthogneisses with subordinate garnet-bearing amphibolites (pink in Fig. 3) occurs; the granitoid protoliths were intrusive within the metavolcanic complex. Hornblende-bearing augen orthogneisses with rare Grt+Cpx amphibolites (red in Fig. 3) are also present in the metaplutonic complex; they show a tonalitic composition and seem to be younger (~530 Ma) than the enclosing orthogneisses (Bauer et al., 2003; Jacobs, 1999). The metaplutonic complex also embeds meter-sized pods of high-grade mafic-ultramafic rocks, some of which are studied here.

3. Methods

Eight mafic-ultramafic samples from Conradgebirge were selected for detailed microstructural, petrological and geochemical studies (Fig. 3). Two of them (28-12-95TF4 and 11-12-95TF3) were analysed by the ^{40}Ar-^{39}Ar method on amphibole and biotite, and one (28-12-95TF4) was modelled through the *P-T* pseudosection technique. All samples are stored in the rock repository of *Museo Nazionale dell'Antartide* (Siena University, Italy; online database: //www.mna.it/english/Collections/collezioni_set.htm).

3.1. Mineral and bulk-rock analyses

Whole-rock major and trace elements (including rare earth elements – REE) analyses were determined by ICP-AES and ICP-MS spectrometry at Actlabs (Ontario, Canada), on a whole-rock powder dissolved through the Li-metaborate and Li-tetraborate fusion method.

Mineral compositions were obtained using SX100 and SXFIVE electron microprobes at *CAMPARIS* (CNRS, Paris, France). The accelerating voltage was 15 kV; the beam current was 40 nA for garnet and 10 nA for the other minerals; natural standards were used for calibration. Structural formulas are calculated on the basis of 23 (amphiboles), 22 (micas), 12 (garnet), 8 (plagioclase), 6 (pyroxenes), 4 (olivine, spinel), or 3 (ilmenite) equivalent oxygens (Tables S1-S5). Fe^{3+} contents are estimated on the basis of 4 cations for 6 oxygens for pyroxenes, and according to Hawthorne et al. (2012) using the excel spreadsheet of Locock (2014) for amphiboles. The nomenclature of Hawthorne et al. (2012) was used for amphibole classification.

3.2. ^{40}Ar-^{39}Ar analyses

Mineral separation and ^{40}Ar-^{39}Ar analyses were completed at IGG-CNR (Pisa, Italy). After crushing and sieving, amphiboles and biotites were concentrated from the 0.35–0.50 mm grain size using standard separation techniques and further purified by hand-picking under a stereomicroscope. Amphibole separates were leached in an ultrasonic bath (at room *T*) for 10 min in HNO_3 1N and for a few minutes in HF

7%. Samples were wrapped in aluminium foil and irradiated for 60 h in the core of the TRIGA reactor at the University of Pavia (Italy) along with the dating standard Fish Canyon sanidine (FCs). After irradiation, samples were placed in an ultrahigh-vacuum laser port and baked overnight at 180°C. ^{40}Ar-^{39}Ar laser step-heating experiments were undertaken using a Nd:YAG infrared laser defocused to a ~2-mm spot size. Steps were carried out at increasing laser power to complete melting. Single grain total-fusion analyses of the fluence monitor FCs (five for each stack position) were carried out using a continuous wave CO_2 laser defocused to 1-mm spot size. After cleanup (10 min, including 1 min of lasering), using two Saes AP10 getters held at 400°C and one C-50 getter held at room *T*, extracted gases were equilibrated by automated valves into a MAP215-50 noble gas mass spectrometer fitted with a Balzers SEV217 secondary electron multiplier. Ar-isotope peak intensities were measured ten times for a total of ~25 min. Blanks were analysed every one to three analyses. Mass discrimination was monitored by analysis of air pipettes and correction factors for interfering isotopes were determined on K- and Ca-rich glasses. Errors are given at 2σ and are quoted for each heating step as analytical errors, including in-run statistics and uncertainties in the discrimination factor, interference corrections and procedural blanks. Errors on total gas ages, on error-weighted mean ages or on ages from isochron calculation are internal errors, and also include uncertainties in the J value. Data corrected for post-irradiation decay, mass discrimination effects, isotopes derived from interference reactions and blanks are listed in Table S6. Ages were calculated using the IUGS recommended constants (Steiger and Jäger, 1977) and an age of 28.03 Ma for FCs (Jourdan and Renne, 2007). We adopted old constants due to the lack of general consensus regarding new ^{40}K decay constants. More details on the analytical procedures can be found in Di Vincenzo and Skála (2009).

3.3. Thermodynamic Modelling

In order to model the *P-T* evolution of the 28-12-95TF4 ultramafic rock, we have calculated various isochemical *P-T* diagrams (or “pseudosections”), using the Thermocalc software package (v 3.40) and the internally-consistent thermodynamic dataset of Holland and Powell (2011; release 6.2 of 2015). We considered the following activity-composition models: silicate melt, purposely designed for the partial melting of metabasic rocks in the NCKFMASH system (Green et al., 2016); clinoamphibole (NCKFMASHTO:

Green et al., 2016); garnet (CMnFMASO: White et al., 2014a, 2014b); calcic augite (NCFMASO: Green et al., 2016), with the complex solid solution Di–Hd–Ca-Ts–clinoferrosilite–clinoenstatite–Jd–Acm; orthopyroxene (CMnFMASO: White et al., 2014a, 2014b); spinel (FMATO: White et al., 2002); biotite (KMnFMASHO: White et al., 2014a, 2014b); plagioclase (NCKAS: Holland and Powell, 2003); ilmenite (FMTO: White et al., 2000, 2014b).

A first *P-T* pseudosection was calculated for the bulk composition of the rock (Fig. 10a, b) and two others for the chemical composition of rock microdomains, namely a cm-sized magmatic clinopyroxene with numerous exsolution lamellae (Fig. 10c) and an inclusion of plagioclase entrapped in garnet (Fig. 10d). The information provided by these pseudosections is presented in Section 7.

4. Petrography and mineral chemistry

Two groups of mafic-ultramafic rocks are distinguished here, on the basis of their geological setting, as well as from a petrological perspective. The first group consists of Cam+Pl+Grt±Cpx±Bt amphibolites and Cpx+Cam±Opx granulitic fels that belong to the metavolcanic complex, from the northern and southern parts of Conradgebirge (Fig. 3). The second group is represented by Grt+Cpx+Cam±Opx granulitic fels and minor Cpx-bearing amphibolites enclosed in the metaplutonic complex, cropping in the central zone of Conradgebirge (Fig. 3).

4.1. Metavolcanic complex

The samples from the metavolcanic complex (10-12-95CF33, 10-12-95TF7, 10-12-95TF8A, 10-12-95TF8B, and 11-12-95TF3) were taken from boudins of a few metres to tens of metres in length, which form discontinuous mafic levels in migmatites of metasedimentary origin, which are in turn interleaved with metavolcanics (Fig. 4a; Colombo and Talarico, 2004). The latter rocks show a main S_2 foliation with a well-visible L_2 lineation, coaxial with the axis of the most pervasive fold generation (D_2 deformation) and grading locally into a marked stretching lineation (Bauer et al., 2004; Colombo and Talarico, 2004). Relicts of isoclinal folds and foliation preserved in mafic enclaves are thought to represent a D_1 deformation structure (Bauer et al., 2004).

Amphibolites (10-12-95TF7, 10-12-95TF8B and 11-12-95TF3) consist of Cam+Pl±Grt±Cpx±Opx±Bt+Qtz with accessory Opm±Ap±Zrn. They are fine- to medium-grained rocks with a granonematoblastic texture marked by the shape preferential orientation of amphibole, biotite flakes, plagioclase and trails of opaque minerals parallel to the main foliation S_2 (Fig. 5a, b). Clinopyroxene is mainly replaced by green/brown nematoblasts of amphibole and so it is a relict with respect to S_2. Garnet crystals are mm-sized, anhedral and fractured porphyroblasts showing resorbed margins (Fig. 5a); they may enclose epidote, plagioclase, quartz, biotite and pargasitic amphibole. Symplectitic Pl+Opx coronas grew at the contacts between garnet and amphibole (Fig. 5a).

Fels (10-12-95CF33, 10-12-95TF8A) are medium-grained ultramafic rocks with sub-polygonal granoblastic and nematoblastic textures. They consist of Cam+Cpx±Opx±Bt±Ol±Spl with accessory Qtz±Pl+Opm±Ap±Zrn. Clinoamphibole, the most abundant mineral, occurs mainly as prismatic brown crystals that coexist with Cpx and Opx, whereas some green amphibole nematoblasts also developed after clinopyroxene (Fig. 5c). Plagioclase is rare and biotite flakes are associated with amphibole. Olivine and green/brown spinel are present in the most ultramafic rocks (Fig. 5d).

Clinoamphibole is mainly pargasite or magnesiohornblende in composition, independently from its microtextural position (Table S1). Spot analyses plot in the Al-rich region of the diagrams of Fig. 6 and reveal a trend parallel to the pargasite-tremolite join, with an important pargasite substitution. The nematoblasts are nearly homogeneous with high Al^{IV} content (~1.02–1.93 atoms per formula unit [a.p.f.u.]) and important A-site occupancy (~0.32–0.76 a.p.f.u). Although there is no clear zonation, lower contents of Al^{IV} and $(Na+K)_A$ are noticeable near the cleavages, where some evolution towards the tremolite end-member may have occurred during retrogression. Amphibole from sample 11-12-95TF3 also shows lower Al^{IV} content and A-site occupancy, with respect to the other samples (Fig. 6), and lies among the low-*P* region in Figure 6c, suggesting a late re-equilibration.

Garnet is a Prp-Grs-rich almandine with a slight X_{Mg} decrease from core to rim (10-12-95TF7: $Prp_{20-16}Alm_{61-68}Grs_{14-12}Sps_{3-4}Adr_{2-0}$; Table S2 and Fig. 7). Clinopyroxene is diopside with low Jd and Ca-Ts substitutions ($Di_{67.4}$ $Hd_{20.4}$ $En_{4.8}$ $Fs_{1.5}$ Ca-Ts_4 Ca-Ti-$Ts_{0.04}$ $Jd_{1.04}$). Orthopyroxene is enstatite (En_{79} Fs_{21}), when in equilibrium with Cpx, Ol, Spl and Cam in the fels, whereas it is richer in iron when it developed lately in the symplectitic coronas between garnet and amphibole (Wo_1 En_{46} Fs_{53}: Table S3). Plagioclase is a nearly homogeneous labradorite ($An_{52–54}$: Table S4), with rare oligoclase-rich rims ($An_{\sim23}$) in garnet-free rocks; on the other hand, plagioclase in the symplectite after garnet is bytownite ($An_{84–89}$). Biotite is a phlogopite with X_{Mg} ranging from ~0.65 up to ~0.78. It shows the highest X_{Mg}-values in the ultramafic fels, where it coexists with olivine (Fo_{74}: Table S5) and brown Cr-bearing spinel ($X_{Mg} \cong 0.54$, $Cr_2O_3 \cong 6.5$ wt%: Table S5).

4.2. Metaplutonic complex

Samples from the metaplutonic complex (7-12-95TF4, 18-12-95TF1B, 28-12-95TF4) belong to m-sized pods boudinaged within highly-strained and strongly-migmatized zones (Fig. 4b; Colombo and Talarico, 2004). The rocks are mafic to ultramafic medium-grained fels with an interlobate granoblastic texture. They consist of Cpx+Opx±Cam±Grt±Pl±Bt±Ol±Spl, with accessory Opm±Qtz±Ap±Zrn, but are much different from each other, in particular in the relative abundances of amphibole versus pyroxene.

In amphibole-rich sample 28-12-95TF4, garnet occurs as cm-sized porphyroblasts with rare inclusions of Cam, Bt, Pl, sulphides and melt products (or “nanogranitoids”) (Fig. 5e). Amphibole is the most abundant mineral; mm-sized strained clinopyroxene grains show exsolution lamellae of Opx, Pl and Cam (Fig. 5f; Section 7.1); one unique relict orthopyroxene crystal, with kink bands, is corroded by amphibole. Abundant symplectites grew at contacts with garnet. A kelyphite with two concentric symplectites occurs between garnet and amphibole (Fig. 5e, g); the inner symplectite, close to garnet, consists of Opx+Pl+Spl±Ol±Bt (kel_i in: Fig. 5e, g; Fig. S1), whereas the outer one, near amphibole, is made of Pl+Opx±Cam_2±Spl±Bt (kel_o in Fig. 5e, g). Plagioclase enclosed in garnet also reacted with the latter to form a Pl+Opx+Spl corona (inset in Fig. 10d). Some mm-thick symplectites, made of Pl+Opx±Cam_2, developed between garnet and clinopyroxene, together with an irregular corona of undeformed orthopyroxene on the clinopyroxene side (Fig. 5e).

In amphibole-lacking sample 18-12-95TF1B, three successive parageneses can be distinguished (Fig. 5h). The first consists of anhedral, large almandine (Grt_1 in Fig. 5h) together with anhedral ilmenite (Ilm_1), pyroxene (Cpx_1), quartz (Qtz_1) and apatite (Ap_1). The second paragenesis developed between Grt_1 and Cpx_1; it consists of a kelyphitic intergrowth of anorthite (An_2) + clinopyroxene (Cpx_2) ± orthopyroxene (Opx_2), together with a coronitic orthopyroxene (Opx_2) on the Cpx_1 side. Finally, a coronitic garnet (Grt_3) grew again as thin films at the contacts An_2-Opx_2, An_2-Cpx_2 and An_2-Ilm_1.

Clinoamphibole in 28-12-95TF4 is always pargasite, independently of its microtextural context (Table S1). It shows the highest Al^{IV} content and A-site occupancy with respect to amphiboles from the metavolcanic complex samples (Fig. 6) and belongs, at least in appearance, to the same trend, parallel to the pargasite-tremolite join (Fig. 6a).

Garnet in 28-12-95TF4 is Alm-rich pyrope (Table S2, Fig. 7) showing a nearly homogeneous core with a plateau-shaped profile (Prp_{44} Alm_{38} Grs_{15} Sps_1 Adr_3), but it displays an abrupt X_{Fe} increase from 80 µm onwards to the edge (up to Prp_{27} Alm_{54} Grs_{13} Sps_3 Adr_0). In the amphibole-lacking sample 18-12-95TF1B, porphyroblastic garnet (Grt_1 in Fig. 5h) is also homogeneous, but it is much richer in almandine (Grt_1: $Prp_{6–5}$ $Alm_{68–71}$ $Grs_{20–19}$ $Sps_{1–2}$ $Adr_{4–3}$) than in the previous rock, which likely reflects the strong difference in Fe-content between the two rocks (Section 5.2); the late coronitic garnet (Grt_3: Prp_{3-4} Alm_{71-72} Grs_{20-21} $Sps_{2-3}$$Adr_{1-3}$) is also homogeneous and much similar to Grt_1.

Clinopyroxenes in both rocks also strongly differ by their X_{Fe} ratio (Table S3), which again reflects differences in bulk Fe-contents: Di_{61} Hd_{18} $En_{7.5}$ $Fs_{2.2}$ Ca-$Ts_{6.4}$ Ca-Ti-$Ts_{1.2}$ $Jd_{1.3}$ (Cam-bearing Mg-rich 28-12-95TF4); $Di_{19–23}$ $Hd_{55–56}$$En_{5.0–3.8}$ $Fs_{1.4–9.6}$ Ca-$Ts_{2.6–1.9}$ Ca-Ti-$Ts_{1.0–0.7}$ $Jd_{1.7–0.0}$ (Cam-free Fe-rich 18-12-95TF1B). They have however a common feature, namely the abundance of exsolution lamellae. In 18-12-95TF1B, Fe-rich clinopyroxene crystals are intergrown with orthopyroxene lamellae (Wo_8 En_{21} Fs_{71}), suggesting that they derived from a subcalcic clinopyroxene; the reverse, i.e. orthopyroxene with abundant clinopyroxene intergrowths, although rare, also exists and suggests the former existence of HT pigeonite, which is known to be favoured by Fe-rich compositions (e.g. Davidson and Lindsley, 1985). In 28-12-95TF4, the exsolution lamellae within clinopyroxene are of orthopyroxene (Wo_1 En_{64} Fs_{35}), plagioclase (An_{94}) and pargasitic amphibole. The composition of the proto-pyroxene before exsolution was reconstructed by averaging 500 contiguous areas (18 µm × 18 µm) scanned by the electron beam of the microprobe during acquisition. It yielded a subcalcic clinopyroxene with a high content of Ca-Tschermak ($Di_{42.8}$ $Hd_{16.6}$ $En_{15.3}$ $Fs_{5.9}$ Ca-$Ts_{15.5}$ Ca-

Ti-$Ts_{1.3}$ $Jd_{2.5}$: bulk in Table S3). The unique relict pre-peak kinked orthopyroxene observed in this rock also shows a high Al_2O_3-content ($Wo_{1-0.7}$ En_{69-71} Fs_{29-28}; $Al_2O_3 \cong 3.28–3.42$ wt%; Table S3).

The Opx+Pl-bearing symplectites and coronas that formed between garnet and Cam, Cpx or Pl_1 are made up of An-rich plagioclase and ferromagnesian minerals with relatively high X_{Fe} values, likely inherited from that of garnet (Tables S3-S5). For example, the symplectite at the contact Grt-Cam (28-12-95TF4) consists of Opx ($Wo_1En_{66}Fs_{33}$), rare hyalosideritic olivine ($Fo_{53–54}$), hercynite ($Hc_{59}Spl_{38}Mag_3$) and abundant An-rich plagioclase (An_{93-97}).

5. Whole-rock geochemical data

In order to comprehend the geochemical affinity of the protoliths, bulk-rock analyses of major and trace elements have been carried out on selected samples of mafic-ultramafic rocks from the two above complexes (Table 1; see Section 3.1 for the method). Leaving Na_2O and K_2O aside, because of their mobility during metamorphism, the major components show a great variability, not only between rocks from the two complexes but also within the same complex (Table 1).

5.1. Metavolcanic complex

Assuming an original Fe_2O_3/FeO ratio of 0.15, the CIPW-norm calculation of the metavolcanic complex samples yields Ne-normative norms ranging from olivine websterite to olivine gabbro. All samples show Ni and Cr contents positively correlated with MgO and negatively correlated with Al_2O_3 (Fig. S2), suggesting a cogenetic origin, being the sample 10-12-95CF33 the most primitive (i.e. olivine websterite) and sample 10-12-95TF8B the most evolved (i.e. olivine gabbro). Indeed, the first one displays the lowest Al_2O_3 and CaO (7.24 and 3.21 wt%, respectively) and the highest Fe_2O_3 and MgO (14.82 and 26.17 wt%, respectively), together with high Cr, Ni and Co contents (2440, 930, 109 ppm, respectively). TiO_2 is low or very low (0.624–0.067 wt%). REE contents are very low to moderate ($\Sigma_{REE} \approx 2–76$ ppm). Except for sample 10-12-95TF8A, the REE chondrite-normalized patterns (Fig. 8) show a moderate LREE enrichment ($[La/Sm]_N = 1.3–2.2$), Eu anomalies ranging from slightly negative (Eu/Eu*= 0.8–0.9) to slightly positive (1.04), and a slight HREE fractionation ($[Gd/Yb]_N = 1.4–1.6$). Sample 10-12-95TF8A yields the lowest REE content ($\Sigma_{REE} \approx 2$ ppm) with an LREE depletion ($[Ce/Sm]_N$ = 0.59), and the same HREE fractionation as the other samples ($[Gd/Yb]_N$ = 1.4).

5.2. Metaplutonic complex

Samples from the mafic-ultramafic boudins within the metaplutonic complex are heterogeneous, yielding varied CIPW norms: olivine websterite (18-12-95TF1B), Hy+Ol gabbro-norite (7-12-95TF4) and olivine gabbro (28-12-95TF4). The two Fe-Ti-V-P-rich samples 7-12-95TF4 and 18-12-95TF1B contrast with the Mg-Cr-Ni-rich ultramafic rock 28-12-95TF4 (Table 1). However, these rocks do not clearly define a trend, since no correlation is detected in the Al_2O_3 versus MgO and Cr versus MgO diagrams (Fig. S2). The REE contents are either low in the Mg-Cr-Ni-rich sample (Σ_{REE} = 31 ppm) or high in the Fe-Ti-V-rich ones (Σ_{REE} = 326–348 ppm; ca. 100×chondritic values: Fig. 8). The REE patterns normalized to chondrite also show a contrasting behaviour between the two types of rocks (Fig. 8): moderate LREE enrichment ($[La/Sm]_N$ = 2), positive Eu anomaly (Eu/Eu* = 1.6) and slight HREE fractionation ($[Gd/Yb]_N$ = 2.4) for the Mg-Cr-Ni-rich sample, contrasting with negative Eu anomaly (Eu/Eu* = 0.5–0.2) and nearly flat pattern (La_N/Sm_N = 1.3–0.5; Gd_N/Yb_N = 2.1–1.5) for the Fe-Ti-rich samples.

6. ^{40}Ar-^{39}Ar data

Polished thin sections of samples 11-12-95TF3 and 28-12-95TF4 were preliminarily investigated under a scanning electron microscope in order to ascertain the occurrence of zircon crystals sufficiently large to be analysed by the U-Pb dating method. Unfortunately, sample 28-12-95TF4 did not show detectable zircon crystals and sample 11-12-95TF3 provided only rare and tiny zircons, commonly smaller than 15 µm in size. As a consequence, the geochronological investigation concentrated on ^{40}Ar-^{39}Ar dating.

Biotite separates from both samples yielded internal discordant age profiles, with total gas ages of ~469 and ~495 Ma for sample 11-12-95TF3 and 28-12-95TF4, respectively (Fig. 9). Age profile from biotite 28-12-95TF4 exhibits an overall saddle shape (Fig. 9). The minimum of the saddle, representing ~65% of the total $^{39}Ar_K$ released, gave a concordant segment (MSWD = 1.1) with an error-weighted mean age of 493.6 ± 2.3 Ma. Biotite 11-12-95TF3 yielded instead a hump-shaped age spectrum (Fig. 9), with anomalously young ages in the low-T steps (68, 135, 240 Ma: Table S6), followed by ages as old as ~494 Ma at intermediate laser power. The age pattern then declines to a concordant segment (MSWD = 1.5; seven consecutive steps, representing ~34% of the total $^{39}Ar_K$ released), yielding a weighted mean age of 484.3 ± 2.1 Ma. Hump-shaped age spectra such as that of biotite 11-12-95TF3 are typical for weakly chloritized biotite (Di Vincenzo et al., 2003). Following the interpretation of Di Vincenzo et al. (2003) for comparably shaped patterns, the total gas age represents a minimum estimate of the true biotite ^{40}Ar-^{39}Ar age, and the final concordant segment provides the best estimate.

Amphibole data gave for both samples internally discordant age profiles, with an overall declining shape (Fig. 9) and step-ages ranging nominally from ~5 Ga to ~440 Ma (11-12-95TF3) and from ~1.8 Ga to ~505 Ma (28-12-95TF4). This suggests the presence of trapped parentless ^{40}Ar (excess Ar) in amphibole. Ca/K ratios are constant in both samples for more than 95% of the total $^{39}Ar_K$ released and are in close agreement with those determined by the electron microprobe (Tables S1 and S6). Five consecutive steps from the intermediate- to high-T region in amphibole 28-12-95TF4, representing ~43% of the total $^{39}Ar_K$ released, define a concordant segment (MSWD < 2.0) with a mean age of 506.3 ± 2.6 Ma. Data from amphibole 11-12-95TF3 do not define concordant segments but seven consecutive steps from the intermediate-T region (step 77F to 77O: Table S6), representing ~95% of the total $^{39}Ar_K$ released and characterized by indistinguishable Ca/K ratios, yield a well-defined linear array (MSWD = 0.57) in an $^{36}Ar/^{40}Ar$ versus $^{39}Ar_K/^{40}Ar$ isochron plot (not shown), with an intercept age of 490.1 ± 4.2 Ma and an initial $^{40}Ar/^{36}Ar$ ratio of 2668 ± 199, significantly higher than that of modern atmospheric Ar.

7. Metamorphism and *P-T* evolution

The 28-12-95TF4 rock sample is considered the most relevant to provide the best information on the evolution of Conradgebirge. This metagabbroic rock, mainly composed of Cam+Grt+Cpx, has recorded much of the metamorphic history of the region, as evidenced by various microstructures, such as symplectites around garnet, exsolution lamellae in large clinopyroxene crystals, or even relicts of plagioclase, melt, amphibole and biotite, enclosed in garnet. This rock has also been studied from a geochronological point of view and for “nanogranitoids” preserved in garnet and resulting from partial melting (Ferrero et al., 2017).

7.1. P-T modelling

We proceeded to the thermodynamic modelling of the rock, following a procedure presented in Section 3.3. Three *P-T* pseudosections were modelled:

Bulk rock (Fig. 10a, b) – A first pseudosection was calculated for the bulk composition of the rock, after projection of the minor P_2O_5 component from apatite, a very accessory mineral not considered in the model. The bulk O content has been adjusted so as to give the Fe^{3+} content in amphibole close to the minimum possible value, following the nomenclature of Hawthorne et al. (2012). It has been verified by least squares regression that the resulting composition (in mol%: $[SiO_2]_{45.20}$ $[Al_2O_3]_{9.39}$ $[TiO_2]_{0.76}$ $[MgO]_{20.90}$ $[FeO]_{10.94}$ $[MnO]_{0.16}$ $[CaO]_{10.97}$ $[Na_2O]_{1.03}$ $[K_2O]_{0.57}$ $O_{0.08}$) was a linear combination of the mineral compositions. H_2O saturation is assumed, which seems adequate for such a hydrous rock; it induces a maximum modal abundance of the hydrous phases (amphibole, biotite and melt) without a free aqueous fluid phase coexisting with melt.

Clinopyroxene megacryst (Fig. 10c) – The second pseudosection takes into account the chemical composition of a rock microdomain, namely a 5-mm-sized magmatic clinopyroxene that has exsolved numerous lamellae of orthopyroxene, amphibole and plagioclase (Fig. 5f). The bulk composition of this microdomain was obtained by scanning at the electron microprobe; it is a linear combination of the mineral compositions, as verified by least squares regression: 1 bulk [basis of O_6] = 0.754 Cpx [O_6] + 0.085 Opx [O_6] + 0.088 An [O_8] + 0.013 Cam [$O_{22}(OH)_2$]) + Residuals (very low). Bulk H_2O and O (i.e. Fe^{3+}) contents were deduced from those of the minerals, previously estimated by stoichiometry; these values thus represent the current H_2O and O content of the microdomain, but it should be borne in mind that these may have evolved during the history of the rock. Because the activity-composition model for clinopyroxene does not consider Cr_2O_3 and MnO (Section 3.1), we decided to sum these minor components to Al_2O_3 and FeO, respectively. The composition that was used for calculating the pseudosection of Figure 10c is thus (in mol%): $[SiO_2]_{48.05}$ $[Al_2O_3]_{4.64}$ $[TiO_2]_{0.33}$ $[MgO]_{18.86}$ $[FeO]_{7.43}$ $[CaO]_{19.57}$ $[Na_2O]_{0.33}$ $[K_2O]_{0.05}$$[H_2O]_{0.34}$ $O_{0.41}$.

Plagioclase inclusion (Fig. 10d) – The third pseudosection considers the chemical composition of another microdomain, a 0.5-mm-sized inclusion of plagioclase entrapped in a garnet crystal during its growth (Fig. 5e; inset of Fig. 10d). This plagioclase (An_{51}) reacted with the host garnet during the retrograde evolution to produce an Opx+Spl+Pl corona. The reaction was balanced by the least squares method (see R4 below), and the overall composition of the reactants is very close to that of the products (i.e. the residuals are very low), indicating that the reaction effectively occurred in an almost closed system, although the kelyphite that developed late at the expense of the garnet reached the plagioclase (Fig. 5e). The bulk composition of the reactants (in mol%: $[SiO_2]_{44.77}$ $[Al_2O_3]_{14.74}$ $[MgO]_{14.62}$ $[FeO]_{17.09}$ $[MnO]_{0.52}$ $[CaO]_{7.65}$ $[Na_2O]_{0.60}$ $O_{0.01}$) was therefore retained as representative of the reaction microdomain to be modelled (Fig. 10d).

7.2. P-T evolution

The comparison between the three above models and the observed features allows clarifying the *P-T* evolution of the rock – and, to a certain extent, of the region. Several steps of the rock evolution, indicated by the red arrow in Fig. 10, can be unravelled in this way.

Magmatic crystallization – The modelled rock derives from a gabbroic magmatic rock, as attested by its chemical composition (Table 1) and norm. However, only the mm-sized crystal of clinopyroxene with numerous exsolution lamellae of plagioclase, orthopyroxene and amphibole (Fig. 5e, f) can be considered as inherited from the magmatic stage. The overall composition of this microdomain, obtained by scanning with the electron microprobe, indicates that the pre-exsolution Cpx was Al-rich and subcalcic ($Di_{42.8}$ $Hd_{16.6}$ $En_{15.3}$ $Fs_{5.9}$ Ca-$Ts_{15.5}$ Ca-Ti-$Ts_{1.3}$ $Jd_{2.5}$), which is a typical feature of an HT magmatic pyroxene. Indeed, the *P-T* pseudosection calculated for this domain (Fig. 10c) indicates that abundant (>90 mol%) Tschermak-rich and Ca-poor Cpx is stable with little plagioclase in the presence of a liquid at low *P* and high *T* (>1050°C).

Prograde evolution – Plagioclase, clinoamphibole, biotite and melt inclusions in garnet may help to unravel the prograde metamorphic evolution of the rock. These inclusions were incorporated into garnet during its growth, thus at increasing *P* as indicated by the isomodal curves of garnet (Fig. 10b). The inclusion of plagioclase that was used to model the pseudosection of Fig. 10d provides most of the information. Its composition (An_{51}) implies that it is not of magmatic origin, as it is far removed from the composition obtained by the modelling of the bulk rock for plagioclase in equilibrium with melt at high *T* and low *P* (An_{90-98}: Fig. 10b), as well as from the An_{79} composition obtained for the gabbroic plagioclase by CIPW-norm calculation. On the other hand, the existence of such an intermediate plagioclase, in equilibrium with the paragenesis Cam+Grt+Pl+Chl+Bt±Ep, is predicted for low *P*-*T* conditions (*T* < 550°C, *P* < 0.6 GPa: Fig. 10a). Such a plagioclase effectively matches the observed An_{51} composition at ca. 500°C and 0.5 GPa (An_{51} isopleth in Fig. 10a; star in Fig. 10d). The modelling of the Pl+Grt microdomain (Fig. 10d) constrains the prograde *P*-*T* path, which should have evolved within the large Grt_1+Pl_1(An_{51}) field without overstepping the HP Cpx+Grt+Pl field, where omphacite should appear and plagioclase change its composition (Fig. 10d), which, indeed, did not occur.

The other mineral inclusions observed in garnet, namely biotite and amphibole, provide less rigid constraints on the prograde *P*-*T* path: they were included during garnet growth, thus at increasing *P*, under medium *P*-*T* conditions at which these minerals are stable with garnet (Fig. 10a). The Bt+Grt association is limited towards high *P* by Phg+Rt-bearing parageneses (not shown).

Melt inclusions of “primary origin”, i.e. formed during garnet growth, indicate that the solidus curve of Fig. 10a was overstepped. Ferrero et al. (2017) assessed the composition of one of these melt inclusions. They ascertained that it was enclosed close to the peak at the end of the prograde path, at a low partial-melting rate (<1%); its chemical composition is in good agreement with what predicted by the model at ca. 1.6 GPa and 870°C.

Finally, a unique corroded mm-sized crystal relict of Opx has been observed in the rock matrix; it shows kink bands contrary to the late Opx in symplectites and coronas, from which it also differs in composition. It should have been stable at some stage during the prograde history, implying a prograde *P*-*T* path that crosses some Opx-bearing fields of the *P*-*T* pseudosection (Fig. 10a).

<u>Peak of metamorphism</u> – The phase assemblage inferred to be stable during the peak of metamorphism includes garnet, augite and amphibole, which are abundant in the rock matrix. Nanogranitoid inclusions indicate that melt was also part of the peak assemblage (Ferrero et al., 2017), which should then be defined as Cam+Aug+Grt+Liq±Bt. This paragenesis occupies a wide field in the modelled pseudosection, at *T* >

860°C and P > 1.2 GPa (Fig. 10a). The peak P-T conditions can be further refined using phase compositions, in particular that of garnet. Apart from their edges, the cm-sized garnet crystals display a flat zoning pattern, which should be due to diffusive re-equilibration at high T: Caddick et al. (2010; e.g. Fig. 4) have demonstrated that the growth zoning of a cm-sized garnet totally resets within 0.6 Ma at 900°C. Therefore, the plateau-like core reflects the re-equilibrated garnet close to the peak, and its X_{Fe} isopleth (X_{Fe} = Fe/[Mg+Fe] = 0.490 ± 0.005) constrains the peak P-T conditions between ca. 950°C–2.1 GPa and 970°C–1.5 GPa (Fig. 10b). The need to preserve the An_{51} plagioclase included in garnet (Section 7.1) further restrict these conditions around 1.5–1.7 GPa and 960–970°C (Fig. 10d). Under these conditions, X_{Ca} in garnet would ideally equal 0.17, whereas the real value is 0.160 ± 0.001; the other compositional parameters of the minerals predicted by the model also show a fairly good match with those measured, except for X_{Fe} in amphibole (0.22, instead of 0.29), which likely partially re-equilibrated during retrogression, together with the garnet edges.

Low-P medium-T stage – This stage is evidenced by abundant symplectites that partially replaced garnet. The most remarkable is the "kelyphite" that developed statically at the contacts between garnet and amphibole. It consists in two concentric symplectites, Spl-rich after garnet and Spl-poor after amphibole (Fig. 5e, g), and resulted from a metamorphic reaction that can be roughly balanced through the least-square method:

R1: 1 Cam_1 (basis of $O_{22}[OH]_2$) + 1.16 Grt (Alm_{41} Prp_{43} Grs_{15} Sps_1; O_{12}) → 3.25 Opx (En_{66}; O_6) + 1.78 Pl (An_{94}; O_8) + 0.51 Spl (Hc_{59} Spl_{38} Mag_3; O_4) + 1.00 H_2O (with quite high residuals).

However, this general reaction is commonly complicated by the presence, in the symplectite, of secondary amphibole, among the reaction products. Olivine (Fo_{54}) also developed very locally, apparently replacing orthopyroxene in the symplectite, as suggested by microstructures (Fig. S1) and stoichiometry:

R2: 0.85 Opx + 0.22 Spl → 1 Ol + 0.26 Pl (with high residuals, particularly $Ca_{-0.23}$).

The kelyphite indicates an evolution towards the Opx+Pl+Spl±Grt±Cam±Bt fields that occur at low-P (<0.5 GPa) but still HT (>800°C) conditions in the P-T pseudosection modelled for the bulk-rock composition (Fig. 10a and b). It should be noted here that this evolution involves a P-T path that intersects the X_{Fe} garnet isopleths (Fig. 10b), thus explaining the increase in X_{Fe} (= Fe/[Fe+Mg]) up to 0.64 observed on a thickness of about 80 µm towards the rims of the cm-sized crystals of garnet.

The mm-thick symplectite that developed together with an Opx corona at the contacts between garnet and clinopyroxene (Fig. 5e) formed through the following reaction:

R3: 1 Cpx (O_6) + 0.50 Grt (O_{12}) → 1.10 Opx (O_6) + 0.66 Pl (O_8) (with low residuals).

Again, this symplectite is consistent with an evolution towards Opx+Pl-bearing stability fields, i.e. towards low-*P* medium-*T* conditions (Fig. 10b).

The same evolution is also evidenced by the presence of Opx, Pl and Cam exsolution lamellae in clinopyroxene. The pseudosection of this microdomain suggests that clinopyroxene had first exsolved garnet at the peak of metamorphism (HP region of Fig. 10c). Although no relict of garnet has been observed among the exsolution lamellae, it is obvious that the above reaction R3, which elsewhere developed mm-sized symplectites from Grt and Cpx megacrysts, should have easily removed 50-µm-thick garnet lamellae exsolved in clinopyroxene, to produce the observed composite grains of orthopyroxene and plagioclase, which, in some cases, seem to have inherited the regular shapes of some previous garnet (Fig. 5f). The *P*-*T* model of Fig. 10c indicates that the final Grt-free Cpx+Opx+Pl+Cam paragenesis of this microdomain is stable at P < ~0.5 GPa for a large range of T under 1000°C.

Finally, the relict An_{51} plagioclase (Pl_1) enclosed in garnet reacted with the latter to produce an Opx+Spl+Pl_2 corona of about 300-µm thickness (inset in Fig. 10d). The composition of the garnet (Grt_1) also evolved in contact with this corona, over a thickness of approximately 200 µm (i.e. Grt_2; see the lighter garnet rim in the BSE image of Fig. 10d). This reaction can be balanced as follows:

R4: 1 Grt_1 ($Alm_{44.2}$ $Prp_{37.9}$ $Grs_{16.6}$ $Sps_{1.4}$; O_{12}) + 0.192 Pl_1 ($An_{51.0}$ $Ab_{49.0}$; O_8) → 0.402 Opx ($En_{65.4}$ $Fs_{34.6}$; O_6) + 0.145 Spl ($Hc_{59.0}$ $Spl_{38.1}$ $Mag_{2.5}$ $Gal_{0.4}$; O_4) + 0.396 Pl_2 ($An_{80.7}$ $Ab_{19.3}$; O_8) + 0.615 Grt_2 ($Alm_{52.1}$ $Prp_{31.4}$ $Grs_{13.8}$ $Sps_{2.7}$; O_{12}) (with very low residuals).

The modelling of this microdomain (Fig. 10d) indicates that low-*P* conditions should be reached to produce the observed Opx+Spl+Pl_2(An_{81}) corona. The isopleths for the minerals of the corona (X_{An} in Pl, X_{Fe}

in Opx, X_{Fe} in Spl, etc.) intersect in the *P-T* box 0.35–0.45 GPa and 600–700°C, for relatively high bulk contents of oxygen.

Isobaric cooling – The final evolution towards the surface is poorly documented. Because of the low-*P* conditions of the previous stage, it should have followed a geotherm with a high dT/dP gradient, which is also corroborated by the isopleths for the above microdomain (red arrow Fig. 10d). Some rehydration may have occurred at this stage and can explain the presence of late amphibole among the products of the above symplectites.

8. Discussion

8.1. Nature and origin of the protoliths

In addition to the REE chondrite-normalized patterns of Fig. 8, the discriminating diagrams of Fig. 11, the N-MORB-normalized multi-element spidergram (Fig. 12) and the Th_N versus Nb_N diagram of Fig. 13 help to identify the nature and origin of the protoliths. However, it should be acknowledged that our geochemical study suffers from a lack of samples, obviously difficult to collect in Antarctica, which unfortunately hampers the statistical quality of the results.

Metavolcanic complex – Apart from 10-12-95TF8A, the mafic rocks from the metavolcanic complex show strong Ta-Nb and slight Zr-Hf negative anomalies, together with a positive or negative Ti anomaly and flat HREE patterns (Fig. 12). These features, in particular the Ta-Nb anomaly, together with LREE pattern (Fig. 8), Th/Yb versus Ta/Yb ratios (Fig. 11a) and Ti/V ratio (~4–30: Fig. 11b), point to calc-alkaline rocks, likely formed in an arc/back-arc environment (Fig. 13; Saccani, 2015), and whose magma would have resulted from the extensive partial melting – as suggested by the Zr-Hf negative anomalies (Downes et al., 2015) – of a mantle wedge above a subduction slab. Sample 11-12-95TF3, which falls a little outside the field of calc-alkaline rocks in Fig. 11a, seems also compatible with an arc/back-arc setting, as supported by the Th_N versus Nb_N diagram (Fig. 13) and the Ti/V ratio (~18: Fig. 11b).

The ultramafic rock 10-12-95TF8A shows peculiar characteristics, with a depleted pattern with respect to N-MORB composition, positive Zr-Hf and negative Ti anomalies (Fig. 12). These features, together with a

REE pattern strongly depleted in LREE (Fig. 8), suggest that this rock could be related to a depleted mantle wedge (Bodinier et al., 1984; McDonough and Frey, 1989), likely a back-arc environment (Fig. 13) in an orogenic setting.

Finally, the felsic rocks from the metavolcanic complex have been studied by Jacobs et al. (1998) and Mikhalsky and Jacobs (2004), who assigned them to an early orogenic environment, likely an island arc.

Metaplutonic complex – In the N-MORB-normalized diagram of Fig. 12, the Fe-Ti-rich samples 7-12-95TF4 and 18-12-95TF1B are characterized by higher contents in the most incompatible elements (i.e. Th, Ta, and LREE), nearly similar to those of Ocean Island Basalts (OIB), but they show important Zr-Hf, Eu and Ti negative anomalies, with a flat HREE pattern (Fig. 12). The overall data point to mafic-ultramafic rocks which have some convergence with OIB (Figs. 11 and 13) and could derive from an heterogeneous mantle source with multiple metasomatic events (Lenoir et al., 2000) and repeated partial melting, as suggested by the Zr-Hf, Eu and Ti negative anomalies (David et al., 2000; Lenoir et al., 2000).

As already noted, sample 28-12-95TF4 is quite different. In the diagram of Fig. 12, it also shows enrichment in the most incompatible elements and a slight Zr-Hf negative anomaly, but differs from the previous samples by Eu and Ti positive anomalies. These features reflect a heterogeneous mantle source enriched in highly incompatible trace elements during multiple metasomatic events (David et al., 2000; Downes et al., 2015; Lenoir et al., 2000). Moreover, the analysis falls within the back-arc B field of Fig. 13, suggesting an origin from a mature intra-oceanic back arc without input of subduction (Saccani, 2015).

The mafic-ultramafic samples from the metaplutonic complex, although different, have some common geochemical features: they plot in the mantle-array field of Fig. 11 and are not related to subduction. This is apparently contradictory with the origin suggested for the host orthogneisses: these metagranitoids have a calc-alkaline affinity and would have formed along the same island arc as the metavolcanic complex, which they intruded (Jacobs et al., 1998; Mikhalsky and Jacobs, 2004). In such a context, the mafic-ultramafic boudins could be former xenoliths within the metagranitoids, as suggested by Jacobs et al. (1998, p. 393).

In summary, geochemistry indicates that the felsic and mafic rocks from the metavolcanic complex are linked to subduction and likely related to an arc/back-arc environment. The mafic-ultramafic rocks from the metaplutonic complex show a different origin and are not related to subduction; they could be former xenoliths within metagranitoids.

8.2. Metamorphic evolution and chronology

The thermodynamic modelling of an ultramafic pod of Conradgebirge (28-12-95TF4; Fig. 10) evidences a clockwise *P-T* path with a prograde portion characterized by increasing *T* and *P,* from amphibolite-facies (0.5 GPa; 500°C) up to peak conditions (ca. 1.5–1.7 GPa; 960–970°C). Partial melting is testified by nanogranitoid inclusions enclosed in garnet during its growth (Ferrero et al., 2017). The retrograde path is characterized by an almost isothermal decompression down to ca. 0.5 GPa and 800°C, testified by the static formation of well-developed An+Opx-bearing symplectites around garnet, before a final cooling which did not leave much traces.

This evolution is well documented in mafic-ultramafic boudins preserved within the metaplutonic complex. The main parageneses of most of these rocks are Opx-Pl-free Grt-bearing assemblages, typical of HP-granulite facies (e.g. 28-12-95TF4, 18-12-95TF1B). An+Opx-bearing symplectites and coronas (Fig. 5e, h) indicate a subsequent evolution towards HT low-*P* granulite-facies conditions. A few mafic deformed rocks (e.g. 07-12-95TF4) seem to have recrystallized at this stage. Finally, the last metamorphic evolution consists in an almost isobaric cooling, which led locally to the re-growth of garnet at the expense of the HT symplectites and coronas (18-12-95TF1B; Fig. 5h). The host migmatitic orthogneisses have recorded the last stages of this metamorphic history (Colombo and Talarico, 2004, p. 28-29).

The mafic-ultramafic boudinaged layers observed within the metavolcanic complex do not show much evidence of an HP granulite-facies stage. Very few garnet relicts, corroded by symplectites, recall somehow the early high-grade evolution observed in the ultramafic boudins of the metaplutonic complex. On the other hand, the HT low-*P* granulite-facies stage is here well-documented by Opx+An symplectites, and is likely to be correlated with the similar stage in the metaplutonic complex. The abundance of low-P amphibole (Fig. 6c) and plagioclase, oriented parallel to the main foliation (e.g. 11-12-95TF3; Fig. 5b), indicates that late re-equilibration and deformation under hydrated amphibolite-facies conditions were important here.

At Conradgebirge, several Pan-African ages have been obtained through U-Pb SHRIMP analyses of zircon (Jacobs et al., 1998): (a) a 570-Ma age is attributed to an amphibole-bearing metamorphic stage (M_2) detected in metaplutonic rocks; (b) ages in the range 530–515 Ma are ascribed to a granulite-facies event (M_3), mainly observed in felsic metavolcanic rocks and high-grade Opx-bearing leucosomes; (c) finally, the intrusion of a 512-Ma-old post-tectonic granitoid postdated the previous events. Since the study rocks were unfortunately unsuitable for U-Pb zircon dating, our geochronological constrains are solely based on ^{40}Ar-^{39}Ar mineral ages that necessarily refer to mineral re-equilibration at upper crustal level (T < 650°C). Results indicate for both samples Cambrian to Ordovician ages (506 ± 3 Ma and 494 ± 2 Ma, for amphibole and biotite of sample 28-12-95TF4, respectively; 490 ± 4 Ma and 484 ± 2 Ma, for amphibole and biotite of sample 11-12-95TF3, respectively). A regional comparison within the central DML reveals that ^{40}Ar-^{39}Ar ages from the present work are slightly, though significantly, older than amphibole and biotite ^{40}Ar-^{39}Ar ages obtained for nearby areas to the west (Mühlig–Hofmannfjella and Filchnerfjella, 6–8°E) by Hendriks et al. (2013), who reported ages of ~490–480 Ma for hornblende and ~465–435 for biotite separates. However, our results fall within the second stage of late Neoproterozoic to early Palaeozoic tectono-metamorphic overprint that was recognized on the basis of U–Pb data on igneous and metamorphic rocks from Gjelsvikfjella and Mühlig-Hofmann-Gebirge (~3–4°E; Jacobs et al., 2003). Furthermore, Ar data match remarkably with those from garnet-bearing amphibolites and gneisses from the H.U. Sverdrupfjella area (western DML, 0°30’W–1°30’E), where hornblende yielded ^{40}Ar-^{39}Ar ages in the 500–480-Ma range (Board et al., 2005).

8.3. Geodynamic implications

From the above observations, the following scenario can be proposed as regards the geodynamic history of Conradgebirge, and hence of central DML. The protoliths of the metavolcanic rocks, mostly felsic and subordinately mafic in composition, would have formed in an arc/back-arc environment during the Late Mesoproterozoic (1130 Ma: Jacobs et al., 1998), before the continental collision between the Grunehona-Kaapvaal and East-Antarctic cratons (Bauer et al., 2003) related to the Rodinia assembly (Grenville orogeny). The calc-alkaline granitoids of the metaplutonic complex intruded this formation soon after, at ca. 1080 Ma (Jacobs et al., 1998; Mikhalsky and Jacobs, 2004). Their mafic-ultramafic enclaves could be xenoliths taken away from the mantle or lower crust, and derive from magma generated in a metasomatized mantle that underwent extensive partial melting; similar chemical affinities have been reported in the Mesoproterozoic Namaqua-Natal-Maud belt (Hanson et al., 2006). This early evolution of Conradgebirge is in keeping with what observed elsewhere in DML (Bauer et al., 2003; Jacobs et al., 1998, 2015; Satish-Kumar et al., 2008; Shiraishi et al., 1991) and beyond in the Namaqua-Natal belt (e.g. Grantham et al., 1997; Jacobs et al., 2008; Thomas et al., 1994). Apart from a possible metamorphic event at ca. 1080 Ma (M_1: Jacobs et al., 1998), most of the metamorphic evolution of the Conradgebirge is ascribable to the Pan-African orogeny (Section 8.2), with a well-documented clockwise *P-T* path (Section 7.2), which can be explained in terms of subduction and/or continental collision (e.g. Harley et al., 2013).

In this general frame, a question remains unsettled: the age of the earlier metamorphic phase(s), named M_1 (and M_2) by Rakivant et al. (1997) and Jacobs et al. (1998), and preserved in the ultramafic enclaves of central DML. If they predate the 1.08-Ga-old intrusion of the host metagranitoids, these episodes would be related to the Grenville orogeny. These rocks have recorded two well-distinct high-grade episodes (Sections 7.2 and 8.2): (a) a peak metamorphism in HP-HT granulite-facies conditions, corresponding to the main Grt+Cpx±Cam paragenesis, without plagioclase or orthopyroxene, and preserved in undeformed nuclei; (b) a later stage of low-*P* granulite-facies metamorphism, resulting in the growth of abundant symplectites and coronas made of Opx±Spl+Pl (An-rich); when deformation (D_3) occurred at this stage, the rock recrystallized to give a foliated assemblage with Cpx+Opx+Pl±Cam but without garnet (e.g. 7-12-95TF4). While reconstructing the *P-T* path of sample 28-12-95TF4, we have opted for a gradual transition between these two stages (red arrow in Fig. 10). However, it is possible that they actually belong to two orogenic cycles, Grenville and Pan-African, which the petrological study cannot make it possible to evidence in the absence of geochronological data. This hypothesis is reinforced by taking into consideration the host metagranitoids, whose ability to hold out, without intensive melting, the high *T* (up to 960°C) recorded by the enclaves can be questioned and whose main metamorphic stage with Opx+Pl-bearing foliated assemblages (M_3: Jacobs et al., 1998; Colombo and Talarico, 2004) are apparently related to the low-*P* granulite-facies stage (i.e. the kelyphites) in the enclaves.

Some responses are to be found in other areas of DML and East Antarctica. Eclogites and mafic HP granulites have been suspected to occur in different localities of DML – mostly in western DML (see reviews in: Godard and Palmeri, 2013; Pauly et al., 2016). The most convincing and documented occurrences are from H.U. Sverdrupfjella (western DML), where retrogressed eclogites have been found (Groenewald, 1995; Board et al., 2005), with a reported HP-metamorphism age of ~565 Ma (Board et al., 2005). Felsic HP granulites from the same region allowed Pauly et al. (2016) inferring a *P-T* evolution very similar to that we deduced from the 28-12-95TF4 mafic enclave, and they proposed an age of 570 ± 7 Ma, mainly based on monazite and zircon dating, for the metamorphic peak. Pauly et al.'s study makes it possible to assert that the HP granulite-facies metamorphism is linked to the Pan-African orogeny and that felsic rocks, if sufficiently anhydrous, can undergo high temperatures without intensive melting. Finally, the ultramafic eclogite-facies rocks of Shackleton Range (Schmädicke and Will, 2006; Romer et al., 2009; Will et al., 2009), which occur further south following the extension of the Mozambique belt, are also attributed to the Pan-African orogenic cycle (525–520 Ma: Romer et al., 2009).

By analogy with those examples, the HP granulite-facies metamorphism (M_2) at Conradgebirge should likely be ascribed to the Pan-African orogen. However, the earlier magmatic and amphibolite-facies (M_1?) stages, testified respectively by Cpx megacrysts and Pl (An_{51}) relicts in sample 28-12-95TF4 (Section 7.2), might be Grenvillian. The whole clockwise *P-T* path can be explained by lithosphere doubling and heating (M_2: HP peak) followed by nearly isothermal uplift (M_3: Opx+Pl-bearing kelyphites) before an almost isobaric cooling (M_4). Major transpressive sinistral shear zones (e.g. SOSZ in Fig. 2) could have favoured the M_3-D_3 exhumation phase, similarly to what suggested about the Heimefront shear zone (Jacobs and Thomas, 2004) considered to be responsible for the rapid decompression of the HP granulites in H.U. Sverdrupfjella (Pauly et al., 2016). This tectono-metamorphic scenario is here related to the collision between the East-Gondwana and West-Gondwana blocks that led to the formation of the Mozambique orogenic belt and the final assembly of Gondwana.

9. Conclusions

Our study on mafic-ultramafic rocks from Conradgebirge in central DML (East Antarctica), together with previously published results, leads to the main following conclusions:

(a) The ultramafic rock 28-12-95TF4 recorded a clockwise *P-T* path that reached HP granulite-facies conditions and culminated at ca. 960°C and 1.7 GPa. It has undergone a partial melting predicted by thermodynamic modelling and attested by the presence of “nanogranitoid” micro-inclusions derived from melt entrapped within garnet. The amphibole-rich paragenesis at the metamorphic peak consists of pargasite+Grt+Cpx, with very few relicts of Pl and Opx. The decompression towards low-*P* granulite facies is evidenced by the resorption of garnet and the appearance of Opx and An-rich plagioclase in the form of symplectites.

(b) Mesoproterozoic volcanics and granitoids, formed in an arc/back-arc environment during the Grenville orogenic cycle, have undergone the above metamorphic evolution, before the final exhumation that occurred at the Cambrian-Ordovician boundary (~505–480 Ma). This tectono-metamorphic history, similar to that evidenced at Sverdrupfjella in western DML, is imputable to the Pan-African orogeny, linked to the continent collision between Africa and East-Antarctica that led to the final Gondwana amalgamation.

Acknowledgements

Rock samples were selected from the collection available at the PNRA (*Programma Nazionale Ricerche in Antartide*) rock repository located at the *Museo Nazionale dell’Antartide* (Siena, Italy). The research was realized with the financial support by PNRA (PdR 13/B2.07).

References

Baldwin, J.A., Bowring, S.A., Williams, M.L., 2003. Petrologic and geochronologic constraints on high-pressure, high-temperature metamorphism in the Snowbird tectonic zone, Canada. Journal of Metamorphic Geology 21, 81-98.

Bauer, W., Jacobs, J., Paech, H.-J., 2004. Structural evolution of the metamorphic basement of central Dronning Maud Land, East Antarctica, in: Paech, H.-J. (Ed.), International GeoMaud Expedition of the BGR to central Dronning Maud Land in 1995-96. Geologisches Jahrbuch B96, 325-363.

Bauer, W., Thomas, R.J., Jacobs, J., 2003. Proterozoic-Cambrian history of Dronning Maud Land in the context of Gondwana assembly, in: Yoshida, M., Windley, B.F., Dasgupta, S. (Eds.), Proterozoic East Gondwana: supercontinent assembly and breakup. Geological Society of London, Special Publications 206, pp. 247-269.

Black, L.P., Harley, S.L., Sun, S.S., McCulloch, M.T., 1987. The Rayner Complex of East Antarctica: complex isotopic systematics within a Proterozoic mobile belt. Journal of Metamorphic Geology 5, 1-26.

Board, W.S., Frimmel, H.E., Armstrong, R.A., 2005. Pan-African tectonism in the western Maud Belt: P-T-t path for high-grade gneisses in the H. U. Sverdrupfjella, East Antarctica. Journal of Petrology 46, 671-699.

Bodinier, J.L., Dupuy, C., Dostal, J., 1984. Geochemistry of Precambrian ophiolites from Bou Azzer, Morocco. Contributions to Mineralogy and Petrology 87, 43-50.

Boger, S.D., 2011. Antarctica before and after Gondwana. Gondwana Research 19, 335-371.

Caddick, M.J., Konopásek, J., Thompson, A.B., 2010. Preservation of Garnet Growth Zoning and the Duration of Prograde Metamorphism. Journal of Petrology 51, 2327-2347.

Colombo, F., Talarico, F.M., 2004. Regional metamorphism in the high-grade basement of central Dronning Maud Land, East Antarctica, in: Paech, H.-J. (Ed.), International GeoMaud Expedition of the BGR to central Dronning Maud Land in 1995-96. Geologisches Jahrbuch B96, 7-47.

David, K., Schiano, P., Allègre, C.J., 2000. Assessment of the Zr-Hf fractionation in oceanic basalts and continental materials during petrogenetic processes. Earth and Planetary Science Letters 178, 285-301.

Davidson, P.M., Lindsley, D.H., 1985. Thermodynamic analysis of quadrilateral pyroxenes. Part II: model calibration from experiments and applications to geothermometry. Contributions to Mineralogy and Petrology 91, 390-404.

Di Vincenzo, G., Viti, C., Rocchi, R., 2003. The effect of chlorite interlayering on ^{40}Ar-^{39}Ar biotite dating: an ^{40}Ar-^{39}Ar laserprobe and TEM investigation of variably chloritised biotites. Contributions to Mineralogy and Petrology 145, 643-658.

Di Vincenzo, G., Skála, R., 2009. ^{40}Ar-^{39}Ar laser dating of tektites from the Cheb Basin (Czech Republic): Evidence for coevality with moldavites and influence of the dating standard on the age of the Ries impact. Geochimica et Cosmochimica Acta 73, 493-513.

Downes, H., de Vries, C., Wittig, N., 2015. Hf-Zr anomalies in clinopyroxene from mantle xenoliths from France and Poland: implications for Lu-Hf dating of spinel peridotite lithospheric mantle. International Journal of Earth Science (Geological Rundschau) 104, 89-102.

Elvevold, S., Engvik, A.K., 2013. Pan-African decompressional P-T path recorded by granulites from central Dronning Maud Land. Mineralogy and Petrology 107, 651-664.

Elvevold, S., Gilotti, J.A., 2000. Pressure-temperature evolution of retrogressed kyanite eclogites. Weinschenk Island, North-East Greenland Caledonides. Lithos 53, 127-147.

Engvik, A.K., Elvevold, S., 2004. Pan-African extension and near-isothermal exhumation of a granulite facies terrain, Dronning Maud Land, Antarctica. Geological Magazine 141, 649-660.

Engvik, A.K., Elvevold, S., Jacobs, J., Tvetene, E., de Azevedo, S., Njange, F., 2007. Pan-African granulites of central Dronning Maud Land and Mozambique: A comparison within the East-African-Antarctic orogen. US Geological Survey and The National Academies, proceedings of X ISAES, USGS OF-2007-1047, Short research paper 065.

Ferrero, S., Palmeri, R., Godard, G., Wunder, B., Cesare, B., 2016. Nanogranitoid inclusions in ultramafic high-pressure granulites from Dronning Maud Land (Antarctica). 2nd European Mineralogical Conference, 11-15 September 2016, Rimini (Italia), Book of Abstracts, p. 276.

Ferrero, S., Godard, G., Palmeri, R., Wunder, B., Cesare, B., 2017. Partial melting of ultramafic granulites from Dronning Maud Land (Antarctica): constraints from melt inclusions and thermodynamic modeling. American Mineralogist, submitted.

Gayk, T., Kleinschrodt, R., Langosch, A., Seidel, E., 1995. Quartz exsolution in clinopyroxenes of high-pressure granulites from the Münchberg massif. European Journal of Mineralogy 7, 1217-1220.

Godard, G., Palmeri, R., 2013. High-pressure metamorphism in Antarctica from Proterozoic to Cenozoic: a review and some geodynamic consequences. Gondwana Research 23, 844-864.

Golynsky, A., Jacob, J., 2001. Grenville-age versus Pan-African magnetic anomaly imprints in western Dronning Maud Land, East Antarctica. Journal of Geology 109, 136-142.

Gose, W.A., Helper, M.A., Connelly, J.N., Hutson, F.E., Dalziel, I.W.D., 1997. Paleomagnetic data and U-Pb isotopic age determinations from Coats Land, Antarctica: implications for late Proterozoic plate reconstructions. Journal of Geophysical Research 102, 7887-7902.

Grantham, G.H., Storey, B.C., Thomas, R.J., Jacobs, J., 1997. The pre-break-up position of Haag Nunataks within Gondwana. Possible correlation in Natal and Dronning Maud Land, in: Ricci, C.A. (Ed.) The Antarctic region: geological evolution and processes, Terra Antartica Publications, Siena, pp. 13-20.

Gray, D.R., Foster, D.A., Meert, J.G., Goscombe, B.D., Armstrong, R., Trouw, R.A.J., Passchier, C.W., 2008. A Damara orogen perspective on the assembly of southwestern Gondwana, in: Pankhurst, R.J., Trouw, R.A.J., de Brito Neves, B.B., de Wit M.J. (Eds.), West Gondwana: Pre-Cenozoic Correlations Across the South Atlantic Region. Geological Society of London, Special Publications 294, pp. 257-278.

Green, E.C.R., White, R.W., Diener, J.F.A., Powell, R., Holland, T.J.B., Palin, R.M., 2016. Activity-composition relations for the calculation of partial melting equilibria in metabasic rocks. Journal of Metamorphic Geology 34, 845-869.

Grew, E.S., Asami, M., Makimoto, H., 1988. Field studies in the eastern Sør Rondane Mountains, East Antarctica, with the 29th Japanese Antarctic Research Expedition (JARE). Antarctic Journal of the United States 23, 44-46.

Groenewald, P.B., Moyes, A.B., Grantham, G.H., Krynauw, J.R., 1995. East Antarctic crustal evolution: geological constraints and modeling in western Dronning Maud Land. Precambrian Research 75, 231-250.

Grunow, A., Hanson, R., Wilson, T., 1996. Were aspects of Pan-African deformation linked to Iapetus opening? Geology 24, 1063-1066.

Hanson, R.E., Harmer, R.E., Blenkinsop, T.G., Bullen, D.S., Dalziel, I.W.D., Gose, W.A., Hall, R.P., Kampunzu, A.B., Key, R.M., Mukwakwami, J., Munyanyiwa, H., Pancake, J.A., Seidel, E.K., Ward, S.E., 2006. Mesoproterozoic intraplate magmatism in the Kalahari craton: a review. Journal of African Earth Sciences 46, 141-167.

Harley, S.L., 1985. Paragenetic and mineral-chemical relationships in orthoamphibole-bearing gneisses from Enderby Land, East Antarctica: a record of Proterozoic uplift. Journal of Metamorphic Geology 3, 179-200.

Harley, S.L., 1989. The origins of granulites: a metamorphic prospective. Geological Magazine 126, 215-247.

Harley, S.L., Fitzsimons I.C.W., Zhao, Y., 2013. Antarctica and supercontinent evolution: historical perspectives, recent advances and unresolved issues, in: Harley, S.L., Fitzsimons, I.C.W., Zhao, Y. (Eds.), Antarctica and supercontinent evolution. Geological Society of London, Special publications 383, pp. 1-34.

Hawthorne, F.C., Oberti, R., Harlow, G.E., Maresch, W.V., Martin, R.F., Schumacher, J.C., Welch, M.D., 2012. IMA report, nomenclature of the amphibole supergroup. American Mineralogist 97, 2031-2048.

Hendriks, B.W.H., Engvik A.K., Elvevold, S., 2013. $^{40}Ar/^{39}Ar$ record of late Pan–African exhumation of a granulite facies terrain, central Dronning Maud Land, East Antarctica. Mineralogy and Petrology 107, 665–677.

Hoffman, P.F., 1991. Did the breakout of Laurentia turn Gondwanaland inside out? Science 252, 1409-1412.

Holland, T.J.B., Powell, R., 2003. Activity-composition relations for phases in petrological calculations: an asymmetric multicomponent formulation. Contributions to Mineralogy and Petrology 145, 492-501.

Holland, T.J.B., Powell, R., 2011. An improved and extended internally-consistent thermodynamic dataset for phases of petrological interest, involving a new equation of state for solids. Journal of Metamorphic Geology 29, 333-383.

Holmes, A., 1951. The sequence of Precambrian orogenic belts in south and central Africa. 28^{th} International Geological Congress (London), 1948, 14, 254-269.

Jacobs, J., 1999. Neoproterozoic/lower Palaeozoic events in central Dronning Maud Land (East Antarctica). Gondwana Research 2, 473-480.

Jacobs, J., Thomas, R.J., 2004. Himalayan-type indenter-escape tectonics model for the southern part of the late Neoproterozoic-early Palaeozoic East-West-Antarctic orogeny. Geology 32, 721-724.

Jacobs, J., Fanning, C.M., Bauer, W., 2003. Timing of Grenville-age vs. Pan-African medium- to high-grade metamorphism in western Dronning Maud Land (East Antarctica) and significance for correlations in Rodinia and Gondwana. Precambrian Research 125, 1-20.

Jacobs, J., Pisarevsky, S., Thomas, R.J., Becker, T., 2008. The Kalahari craton during the assembly and dispersal of Rodinia. Precambrian Research 160, 142-158.

Jacobs, J., Fanning, C.M., Henjes-Kunst, F., Olesh, M., Paech, H.-J., 1998. Continuation of the Mozambique Belt into East Antarctica: Grenville-age metamorphism and polyphase Pan-African high-grade events in central Dronning Maud Land. Journal of Geology 106, 385-406.

Jacobs, J., Elburg, M., Läufer, A., Kleinhanns, I.C., Henjes-Kunst, F., Estrada S., Ruppel, A. S., Damaske, D., Montero, P., Bea, F., 2015. Two distinct Late Mesoproterozoic/early Neoproterozoic basement provinces in central/eastern Dronning Maud Land, East Antarctica: the missing link, 15-21°E. Precambrian Research 265, 249-272.

Jourdan, F., Renne, P.R., 2007. Age calibration of the Fish Canyon sanidine $^{40}Ar/^{39}Ar$ dating standard using primary K-Ar standard. Geochimica et Cosmochimica Acta 71, 387-402.

Kretz, R., 1983. Symbols for rock forming minerals. American Mineralogist 68, 277-279.

Laird, L. Albee, A.L., 1981. Pressure, temperature and time indicators in mafic schists: their application to reconstructing the polymetamorphic history of Vermont. American Journal of Science 281, 127-175.

Lenoir, X., Garrido, C.J., Bodinier, J.L., Dautria, J.M., 2000. Contrasting lithospheric mantle domains beneath the Massif Central (France) revealed by geochemistry of peridotite xenoliths. Earth and Planetary Science Letters 181, 359-375.

Locock, A.J., 2014. An excel spreadsheet to classify chemical analyses of amphiboles following the IMA 2012 recommendations. Computer and Geosciences 62, 1-11.

Makimoto, H., Asami, M., Grew, E.S., 1990. Metamorphic conditions of ultramafic lenses from the eastern Sør Rondane Mountains, Antarctica, in: Kaminuma, K. (Ed.), Proceedings of the NIPR Symposium on Antarctic Geosciences. National Institute of Polar Research, Tokyo, Japan, pp. 9-21.

McDonough, W.F., Frey, F.A., 1989. REE in upper mantle rocks, in: Lipin, B., McKay, G.R. (Eds.), Geochemistry and mineralogy of rare Earths elements. Mineralogical Society of America, pp. 99-145.

Mikhalsky, E, Jacobs, J., 2004. Orthogneisses in central Dronning Maud Land, East Antarctica: their origin and tectonic setting, in: Paech, H.-J. (Ed.), International GeoMaud Expedition of the BGR to central Dronning Maud Land in 1995-96. Geologisches Jahrbuch B96, 49-76.

O'Brien, P.J., Rözler, J., 2003. High-pressure granulites: formation, recovery of peak conditions and implications for tectonics. Journal of Metamorphic Geology 21, 3-20.

Paech, H.-J., Jacobs, J., Bauer, W., Mikhalsky, E., Talarico, F., Colombo, F., Roland, N.W., Henjes-Kunst, F., 2004. Explanatory notes to the 1:500,000 geological map of central Dronning Maud Land, in: Paech, H.-J. (Ed.), International GeoMaud Expedition of the BGR to central Dronning Maud Land in 1995-96. Geologisches Jahrbuch B96, 1 vol. + 4 maps.

Pattison, D.R.M., 2003. Petrogenetic significance of ortho-pyroxene-free garnet+clinopyroxene+plagioclase-bearing metabasites with respect to the amphibolite and granulite facies. Journal of Metamorphic Geology 21, 21-31.

Pauly, J., Marschall, H.R., Meyer, H.P., Chatterjee, N., Monteleone, B., 2016. Prolonged Ediacaran-Cambrian metamorphic history and short-lived high-pressure granulite-facies metamorphism in the H.U. Sverdrupfjella, Dronning Maud Land/East Antarctica): evidence for continental collision during Gondwana assembly. Journal of Petrology 57, 185-228.

Pearce, J.A., 1982. Trace elements characteristic of lavas from destructive plate boundaries, in: Thorpe, R.S. (Ed.), Andesite. John Wiley, New York, pp. 525-548.

Ravikant, V., Bejarniya, B.R., Mukerji, S., Kaul, M.K., 1997. Late Proterozoic granitic orthogneiss from North Payer-Weyprecht Mountains, East Antarctica: their tectono-metamorphic history and regional correlation, in: Ricci, C.A. (Ed.) The Antarctic region: geological evolution and processes, Terra Antartica Publications, Siena, pp. 55-64.

Romer, T., Mezger, K., Schmädicke, E., 2009. Pan-African eclogite facies metamorphism of ultramafic rocks in the Shackleton Range, Antarctica. Journal of Metamorphic Geology 27, 335-347.

Rözler, J., Romer, R.L., 2001. P-T-t evolution of ultrahigh temperature granulites from the Saxon Granulite Massif, Germany. Part I: Petrology. Journal of Petrology 42, 1995-2013.

Saccani, E., 2015. A new method of discriminating different types of post-Archean ophiolitic basalts and their tectonic significance using Th-Nb and Ce-Dy-Yb systematics. Geoscience Frontiers 6, 481-501.

Satish-Kumar, M., Hokada, T., Kawakami, T., Dunkley, D.J., 2008. Geosciences research in East Antarctica (0°-60°E): present status and future perspectives, in: Satish-Kumar, M., Motoyoshi, Y., Osanai, Y., Hiroi, Y., Shiraishi, K. (Eds.), Geodynamic evolution of East Antarctica: a key to the East-West Gondwana connection. Geological Society of London, Special Publications 308, pp. 1-20.

Satish-Kumar, M., Hokada, T., Owada, M., Osanai, Y., Shiraishi, K., 2013. Neoproterozoic orogens amalgamating east Gondwana: did they cross each other? Precambrian Research 234, 1-7.

Schmädicke, E., Will, T.M., 2006. First evidence of eclogite facies metamorphism in the Shackleton Range, Antarctica; trace of a suture between east and west Gondwana? Geology 34, 133-136.

Shackleton, R.M., 1996. The final collision zone between East and West Gondwana. Where is it? Journal of African Earth Sciences 23, 271-287.

Shervais, J.W., 1982. Ti-V plots and the petrogenesis of modern and ophiolitic lavas. Earth and Planetary Science Letters 59, 101-118.

Shiraishi, K., Ellis, D.J., Fanning, C.M., Hiroi, Y., Kagami, H., Motoyoshi, Y., 1997. Re-examination of the metamorphic and protolith ages of the Rayner Complex, Antarctica: Evidence for the Cambrian (Pan-African) regional metamorphic event, in: Ricci, C.A. (Ed.), The Antarctic region; geological evolution and processes; proceedings of the VII international symposium on Antarctic earth sciences. Terra Antartica Publications, Siena, pp. 79-88.

Shiraishi, L., Asami, M., Ishizuka, H., Kojima, S., Osanai, Y., Sakiyama, T., Takahashi, Y., Yamazaki, M., Yoshikura S., 1991. Geology and metamorphism of the Sør Rondane Mountains, East Antarctica, in Thomson, M.R.A., Crame, J.A., Thomson, J.W., (Eds.), Geological evolution of Antarctica, Cambridge University Press, Cambridge, pp. 77-82.

Steiger, R.H., Jäger, E., 1977. Subcommission on Geochronology: convention on the use of decay constants in geo- and cosmochronology. Earth Planetary Science Letters 36, 359-362.

Sun, S.S., McDonough, W.F., 1989. Chemical and isotopic systematic of oceanic basalts: implications for mantle composition and processes, in: Saunders, A.D., Norry, M.J. (Eds.), Magmatism in the Ocean basins. Geological Society of London, Special Publications 42, pp. 315-345.

Thomas, R.J., Agenbacht, A.L.D., Cornell, D.H., Moore, J.M., 1994. The Kibaran of southern Africa: tectonic evolution and metallogeny. Ore Geology Reviews 9, 131-160.

White, R.W., Powell, R., Holland, T.J.B., Worley, B.A., 2000. The effect of TiO_2 and Fe_2O_3 on metapelitic assemblages at greenschist and amphibolite facies conditions: mineral equilibria calculations in the system K_2O-FeO-MgO-Al_2O_3-SiO_2-H_2O-TiO_2-Fe_2O_3. Journal of Metamorphic Geology 18, 497-511.

White, R.W., Powell, R., Clarke, G.L., 2002. The interpretation of reaction textures in Fe-rich metapelitic granulites of the Musgrave Block, central Australia: constraints from mineral equilibria calculations in the system K_2O-FeO-MgO-Al_2O_3-SiO_2-H_2O-TiO_2-Fe_2O_3. Journal of Metamorphic Geology 20, 41-55.

White, R.W., Powell, R., Holland, T.J.B., Johnson, T.E., Green, E.C.R., 2014a. New mineral activity-composition relations for thermodynamic calculations in metapelitic systems. Journal of Metamorphic Geology 32, 261-286.

White, R.W., Powell, R., Johnson, T.E., 2014b. The effect of Mn on mineral stability in metapelites revisited: new a-x relations for manganese-bearing minerals. Journal of Metamorphic Geology 32, 809-828.

Will, T.M., Zeh, A., Gerdes, A., Frimmel, H.E., Millar, I.L., Schmädicke, E., 2009. Palaeoproterozoic to Palaeozoic magmatic and metamorphic events in the Shackleton Range, East Antarctica : constraints from zircon and monazite dating, and implications for the amalgamation of Gondwana. Precambrian Research 172, 25-45.

Zhao, G.C., Cawood, P.A., Wilde, S.A., Lu, L.Z., 2001. High-pressure granulites (retrograded eclogites) from the Hengshan Complex, North China Craton: petrology and tectonic implications. Journal of Petrology 42, 1141-1170.

Figure captions

Fig. 1. Neoproterozoic reconstruction of Gondwana showing the cratonic regions and surrounding mobile belts (modified after Gray et al., 2008). Md: Madagascar; SL: Sri Lanka. The box indicates the central Dronning Maud Land enclosed into the Mozambique belt (580-560 Ma).

Fig. 2. Geological sketch map of central DML (modified after Colombo and Talarico, 2004). Abbreviations in inset map: A Annandagstoppane, B Belgica mountains, HF Heimefrontfjella, KV Kirwanveggen, SR Sør Rondane, SOSZ South Orvin Shear Zone.

Fig. 3. Detailed geological map of Conradgebirge with the location of the study samples.

Fig. 4. a) Mafic boudin in migmatized banded gneiss from the metavolcanic complex, northern Conradgebirge; b) mafic-ultramafic enclave in migmatized orthogneiss (metaplutonic complex) with a late aplitic dyke (central Conradgebirge).

Fig. 5. Microstructures of mafic-ultramafic rocks from Conradgebirge.

a) Resorbed garnet surrounded by a Pl+Opx±Cam symplectite in a matrix consisting of plagioclase, amphibole and biotite; amphibolite 10-12-95TF7 from the metavolcanic complex (VC); plane-polarized light (PPL). b) Amphibolite 11-12-95TF3 from VC with Cam, Pl and Bt as main mineral phases along the main foliation; PPL. c) Amphibole-rich fels with Cpx relicts and rare Pl; sample 10-12-95TF8A from VC; PPL. d) Undeformed Ol+Opx+Cam+Spl fels 10-12-95CF33 from VC; crossed-polarized light (CPL). e) Ultramafic fels 28-12-95TF4 from the metaplutonic complex, showing a porphyroblastic garnet surrounded by kelyphite consisting of an inner (kel_i) zone towards garnet and an outer zone (kel_o) towards amphibole, a relict magmatic Cpx and a large plagioclase formerly enclosed in garnet. The red boxes are the Fig. 5f, 5g and 14d; backscattered-electron (BSE) image. f) Particular of image e, where Cpx shows Opx+Pl (blue and brown) exsolution lamellae along the (010) crystallographic plane, and Cam (green) exsolution lamellae along (100); pink: microfractures and voids; principal component analysis (PCA) elaboration of BSE and element maps. g) Particular of image e, showing the inner kelyphite (kel*i* after garnet) consisting of Opx+Pl+Spl and the outer kelyphite (kel_o after Cam) made of Opx+Pl+Cam_2 but devoid of spinel; PCA elaboration of BSE and element maps. h) Mafic fels 18-12-95TF1B from the metaplutonic complex, showing the peak HP granulite-facies paragenesis (Grt_1 [pink], Qtz_1 [dark green], Cpx_1 [light green], Ilm_1 [grey], apatite [yellow]), from which high-T low-P symplectites (Opx_2 [blue], Cpx_2 [green] and plagioclase An_2 [red]) developed during decompression; very thin coronas of garnet (Grt_3 [pink]) that formed lately at the contacts Opx_2-An_2, Ilm_1-An_2 and Cpx_2-An_2 are interpreted as resulting from the final isobaric cooling; PCA elaboration of BSE and element maps.

Fig. 6. Amphibole composition diagrams of metavolcanic (diamonds) and metaplutonic (squares) complex samples: a) A-site occupancy versus Al^{IV}, b) Al^{IV} versus Al^{VI}, and c) 100×Na/(Na+Ca) versus 100×Al/(Al+Si) after Laird and Albee (1981). All diagrams show a correlation along the tremolite-pargasite join.

Fig. 7. Ca-(Fe+Mn)-Mg diagram for garnet of metavolcanic (diamonds) and metaplutonic (squares) complex samples.

Fig. 8. Bulk-rock trace-elements compositions: REE chondrite-normalized patterns. The La value for sample 10-12-95TF8A is not plotted, being below the detection limit. Chondrite composition from Sun and McDonough (1989).

Fig. 9. ^{40}Ar–^{39}Ar age release spectra for amphibole (a) and biotite (b) separates of samples 11-12-95TF3 and 28-12-95TF4. Box heights indicate the 2σ analytical error.

Fig. 10. *P-T* pseudosections for sample 28-12-95TF4. See sections 3.3 and 7.1 for complete information on the modelling method and parameters. Phases are listed in order of decreasing abundance; those in parentheses are less than 2 mol%; Rt and Ilm may be present in negligible amounts (a, b, c) and can be

ignored. The proposed *P-T* path is evidenced by a red arrow. a) Model of the bulk rock in the NCKMnFMASTO system, with H_2O saturation. b) Particular of the previous model, with isomodal and isopleth curves. c) Model of the microdomain made of Cpx with Pl+Opx+Cam exsolution lamellae (Fig. 5f), in the NCKFMASHTO system. d) Model of the microdomain made of Pl included within Grt, in the NCMnFMASO system; the insert BSE image shows the Pl_2+Opx+Spl corona that developed at the contacts between Pl_1 and the host Grt_1.

Fig. 11. Bulk-rock trace-elements compositions: a) Th/Yb vs. Ta/Yb diagram (Pearce, 1982; compositions of modern N-MORB, E-MORB and OIB from Sun and McDonough, 1989); b) V (ppm) vs. Ti (ppm)/1000 diagram (Shervais, 1982). Abbreviations: TH tholeiitic; CA calc-alkaline; SHO shoshonitic.

Fig. 12. Bulk-rock trace-elements compositions: incompatible multi-element diagram normalized to N-MORB composition (modern N-MORB and OIB compositions, after Sun and McDonough, 1989); the La value for sample 10-12-95TF8A is not plotted, being below the detection limit.

Fig. 13. Tectonic interpretation based on Th_N vs. Nb_N systematics (Saccani, 2015). Backarc A: back-arc basin rocks with input of subduction; backarc B: back-arc basin rocks without input of subduction; OCTZ ocean-continent transition zone. Th and Nb are N-MORB normalized (Sun and McDonough, 1989).

Figure 1

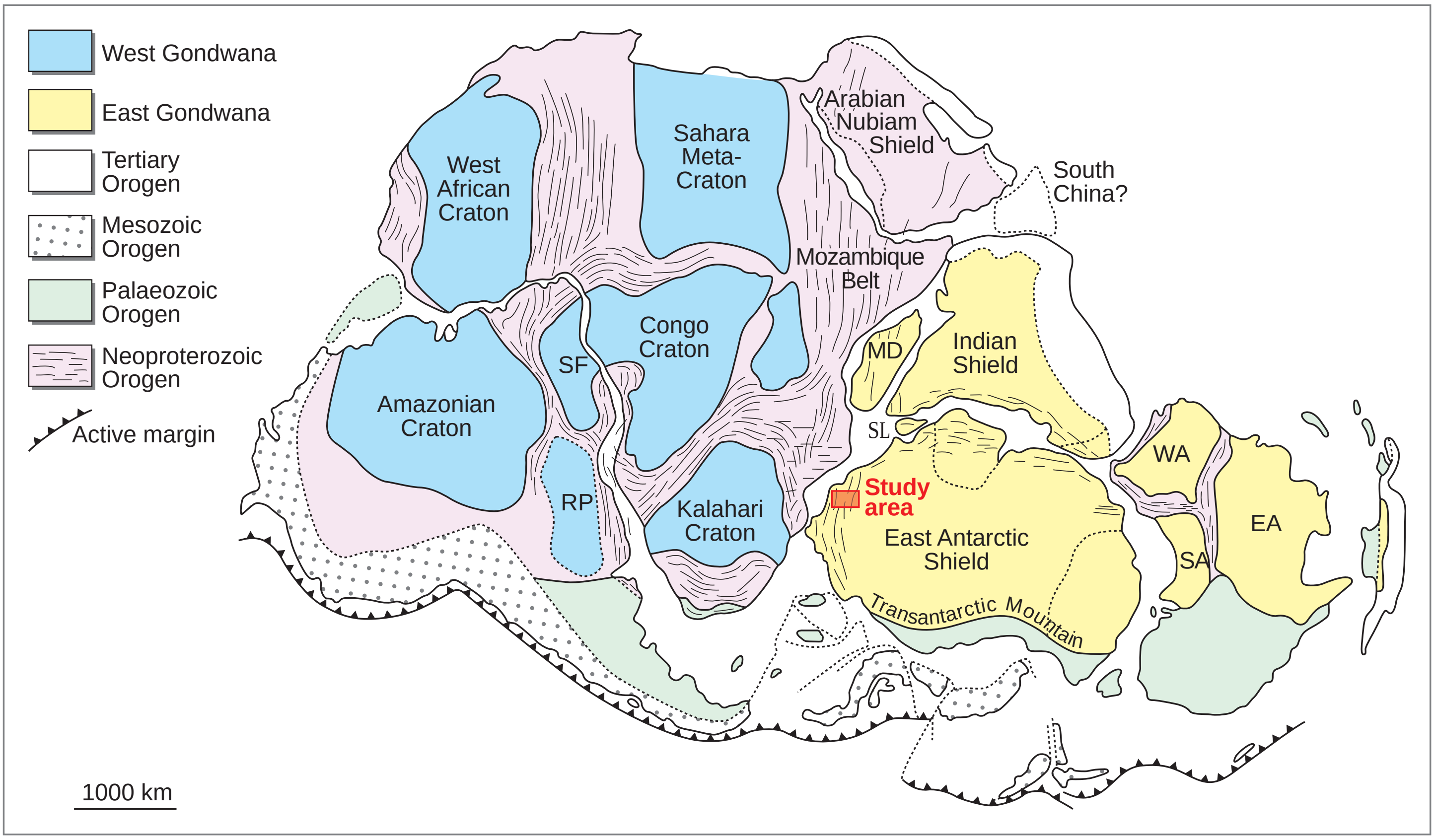

West Gondwana
East Gondwana
Tertiary Orogen
Mesozoic Orogen
Palaeozoic Orogen
Neoproterozoic Orogen
Active margin
1000 km
West African Craton
Sahara Meta-Craton
Arabian Nubiam Shield
South China?
Mozambique Belt
Amazonian Craton
SF
Congo Craton
MD
Indian Shield
SL
RP
Kalahari Craton
Study area
East Antarctic Shield
Transantarctic Mountain
WA
EA
SA

Figure 2
Click here to download high resolution image

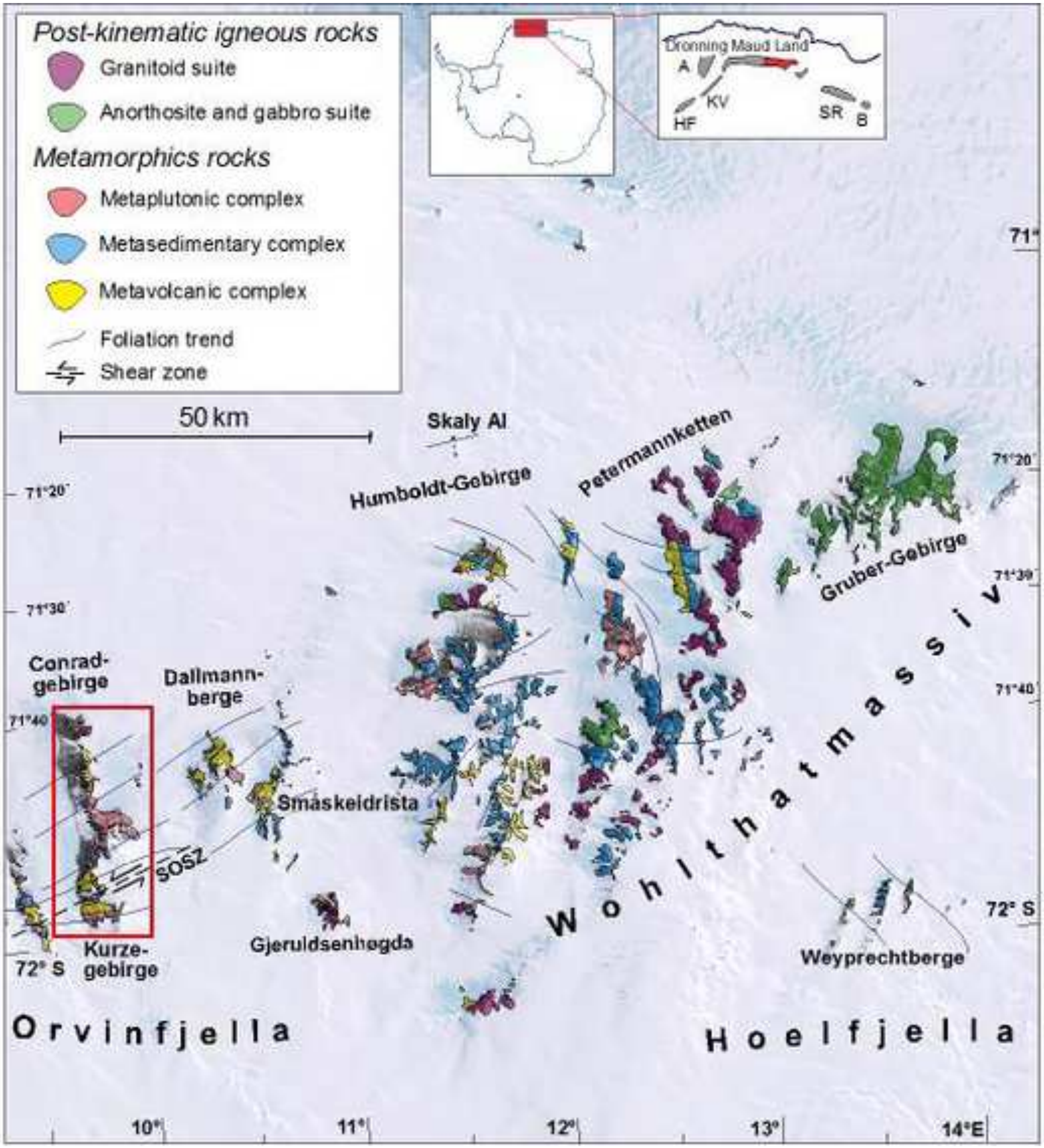

Figure 3

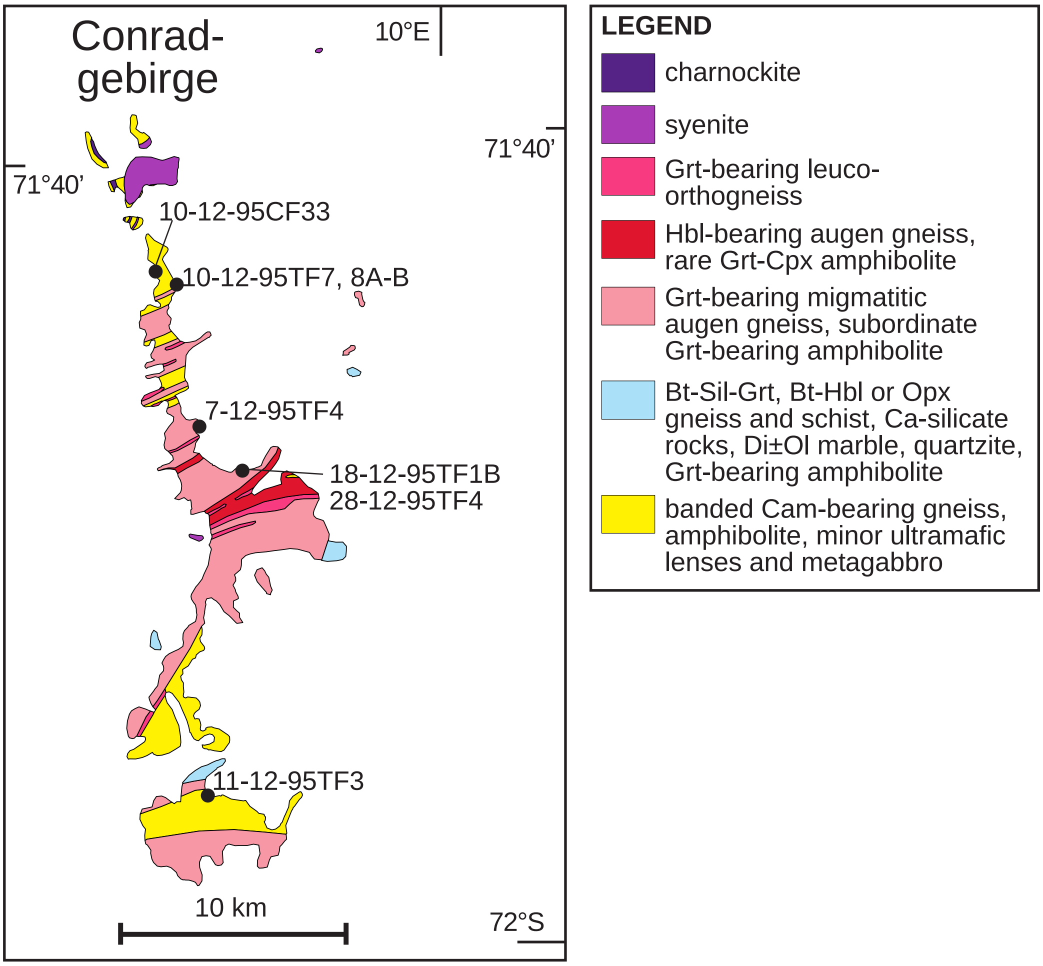
Conrad-
gebirge
10°E
71°40'
71°40'
10-12-95CF33
10-12-95TF7, 8A-B
7-12-95TF4
18-12-95TF1B
28-12-95TF4
11-12-95TF3
10 km
72°S
LEGEND
charnockite
syenite
Grt-bearing leuco-
orthogneiss
Hbl-bearing augen gneiss,
rare Grt-Cpx amphibolite
Grt-bearing migmatitic
augen gneiss, subordinate
Grt-bearing amphibolite
Bt-Sil-Grt, Bt-Hbl or Opx
gneiss and schist, Ca-silicate
rocks, Di±Ol marble, quartzite,
Grt-bearing amphibolite
banded Cam-bearing gneiss,
amphibolite, minor ultramafic
lenses and metagabbro

Figure 4
Click here to download high resolution image

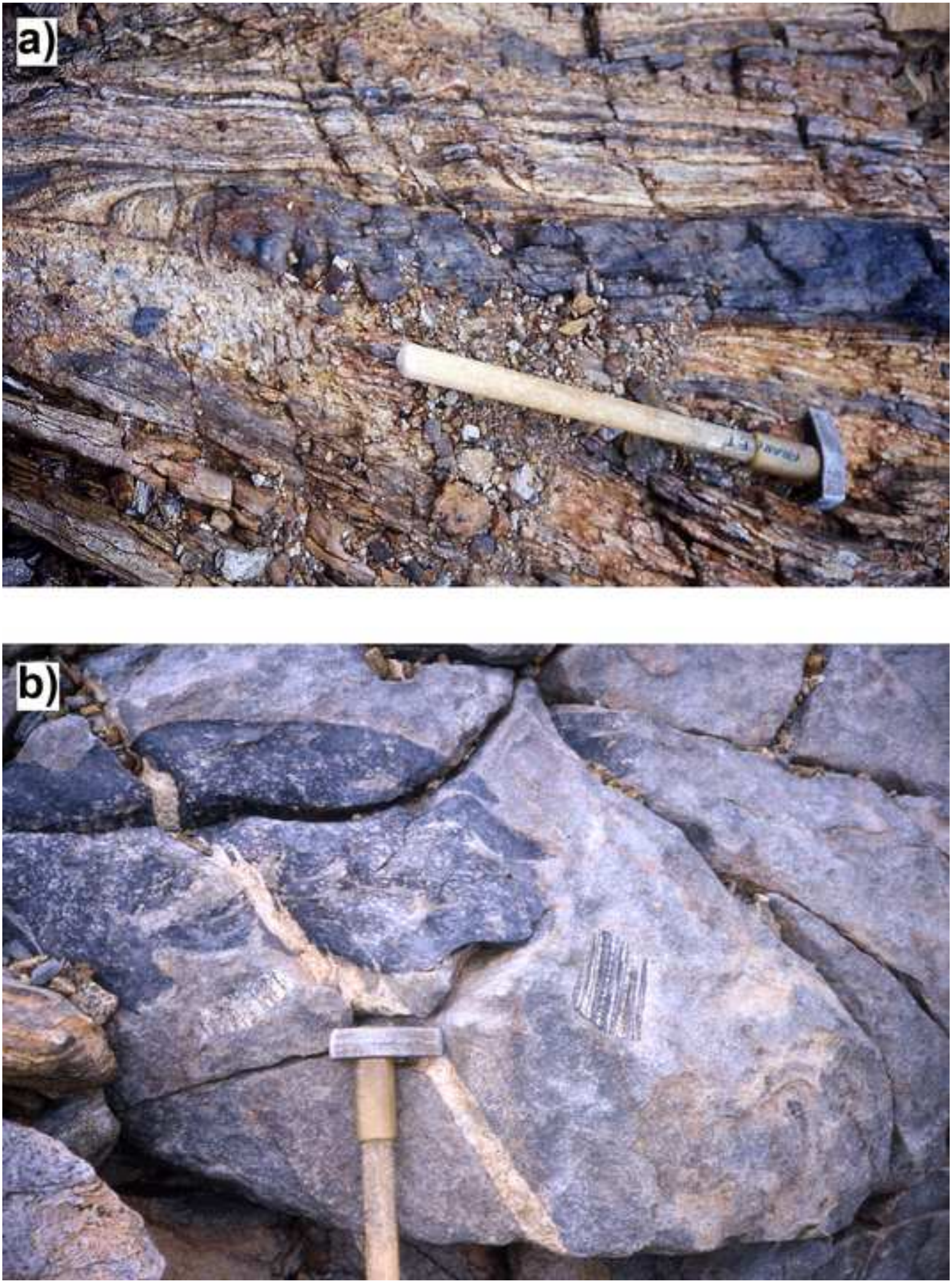

Figure 5

Click here to download high resolution image

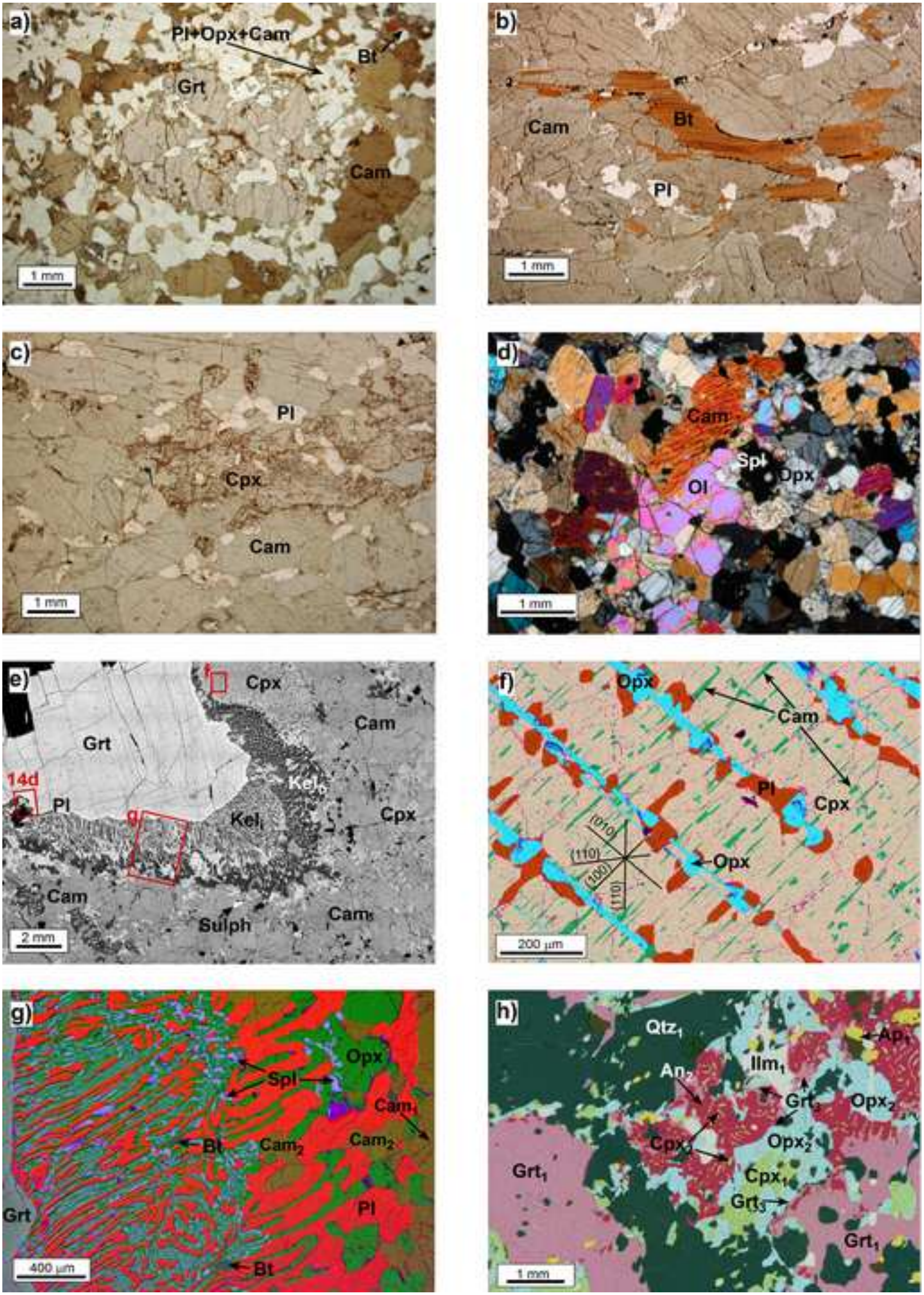

Figure 6

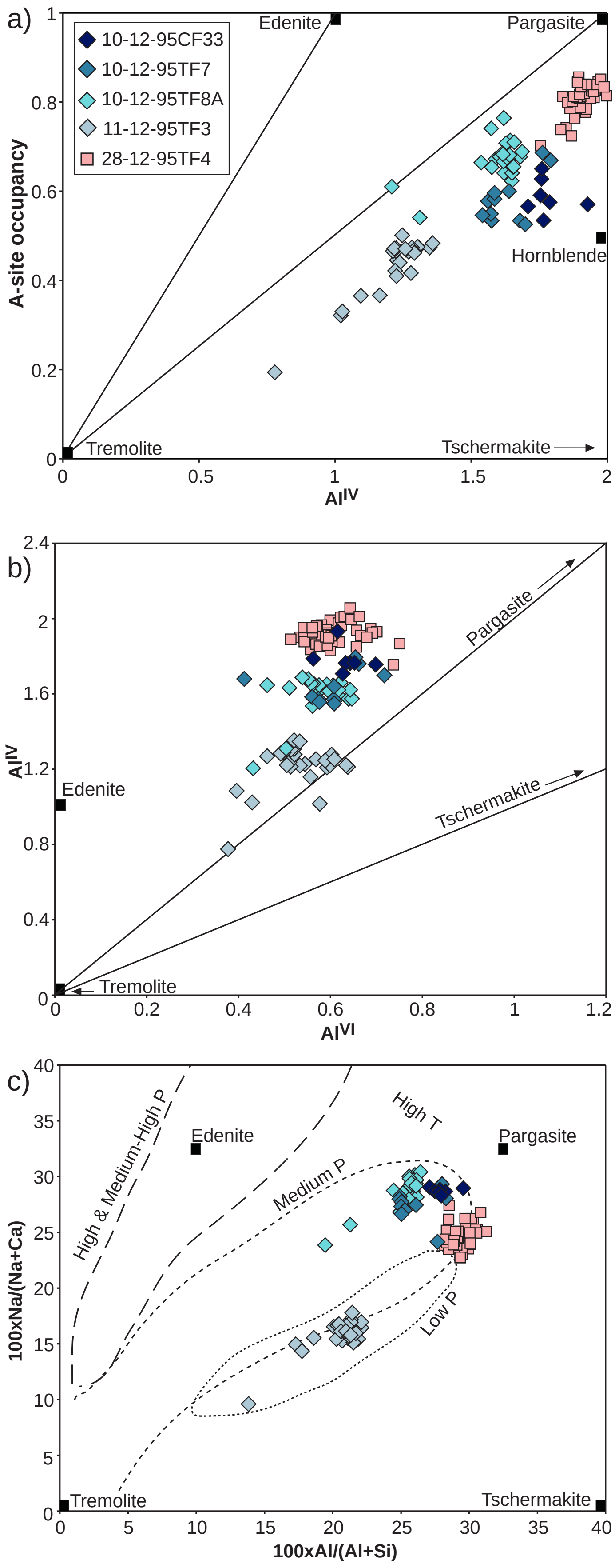
a)
10-12-95CF33
10-12-95TF7
10-12-95TF8A
11-12-95TF3
28-12-95TF4
Edenite
Pargasite
Hornblende
Tremolite
Tschermakite
A-site occupancy
Al^IV
b)
Pargasite
Tschermakite
Edenite
Tremolite
Al^IV
Al^VI
c)
High & Medium-High P
Edenite
High T
Pargasite
Medium P
Low P
Tremolite
Tschermakite
100xNa/(Na+Ca)
100xAl/(Al+Si)

Figure 7

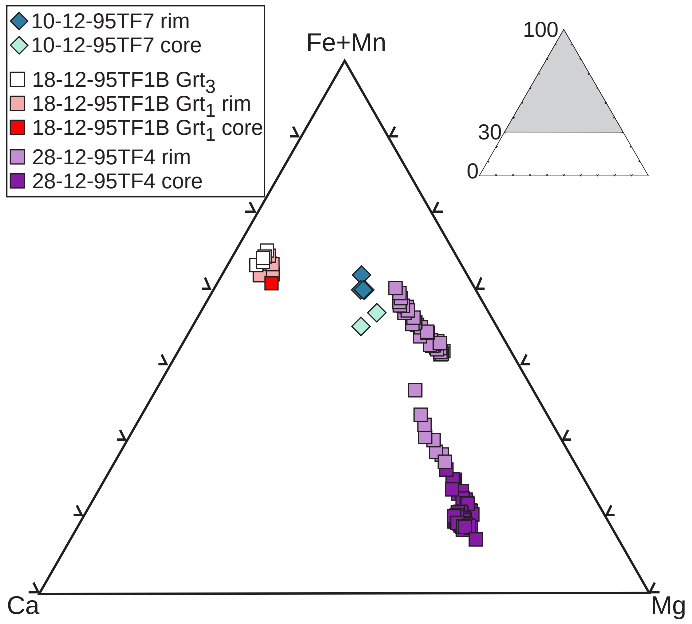

10-12-95TF7 rim
10-12-95TF7 core
18-12-95TF1B Grt3
18-12-95TF1B Grt1 rim
18-12-95TF1B Grt1 core
28-12-95TF4 rim
28-12-95TF4 core
Fe+Mn
Ca
Mg
100
30
0

Figure 8

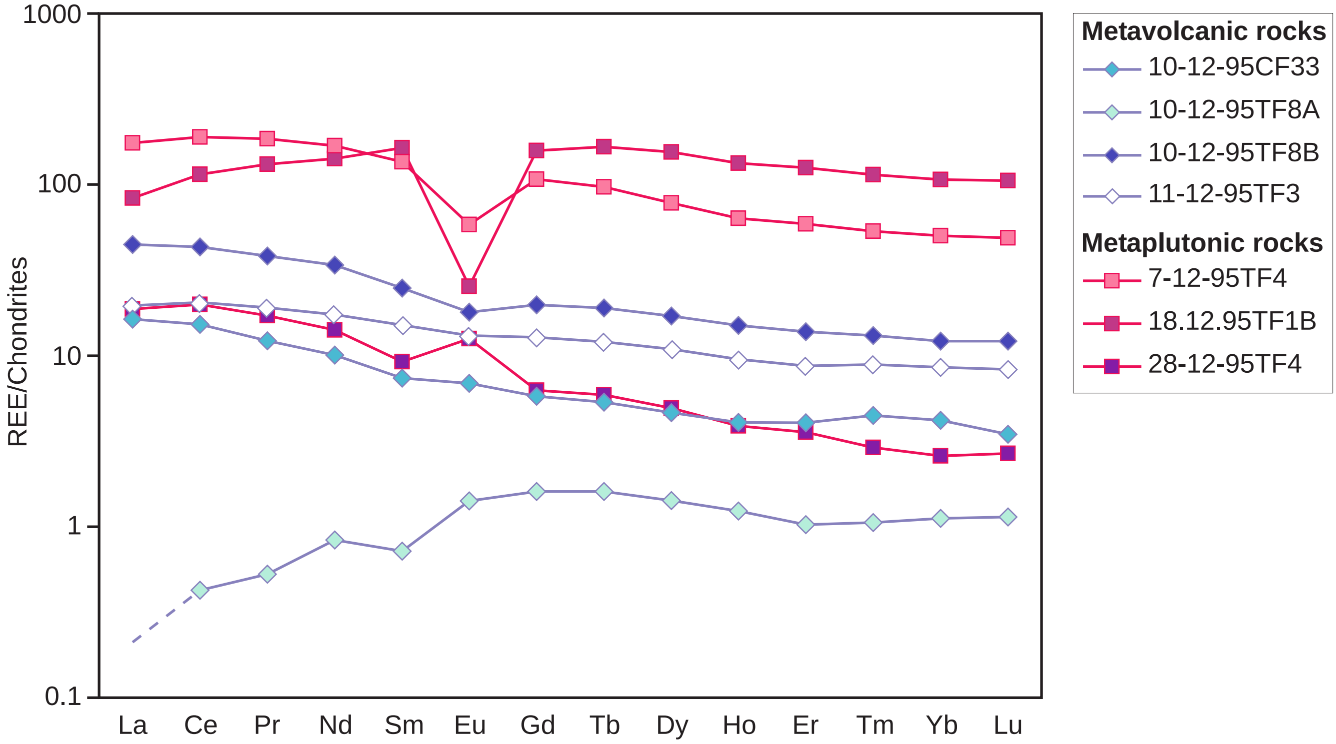

1000
100
10
1
0.1
REE/Chondrites
La
Ce
Pr
Nd
Sm
Eu
Gd
Tb
Dy
Ho
Er
Tm
Yb
Lu
Metavolcanic rocks
10-12-95CF33
10-12-95TF8A
10-12-95TF8B
11-12-95TF3
Metaplutonic rocks
7-12-95TF4
18.12.95TF1B
28-12-95TF4

Figure 9
Click here to download high resolution image

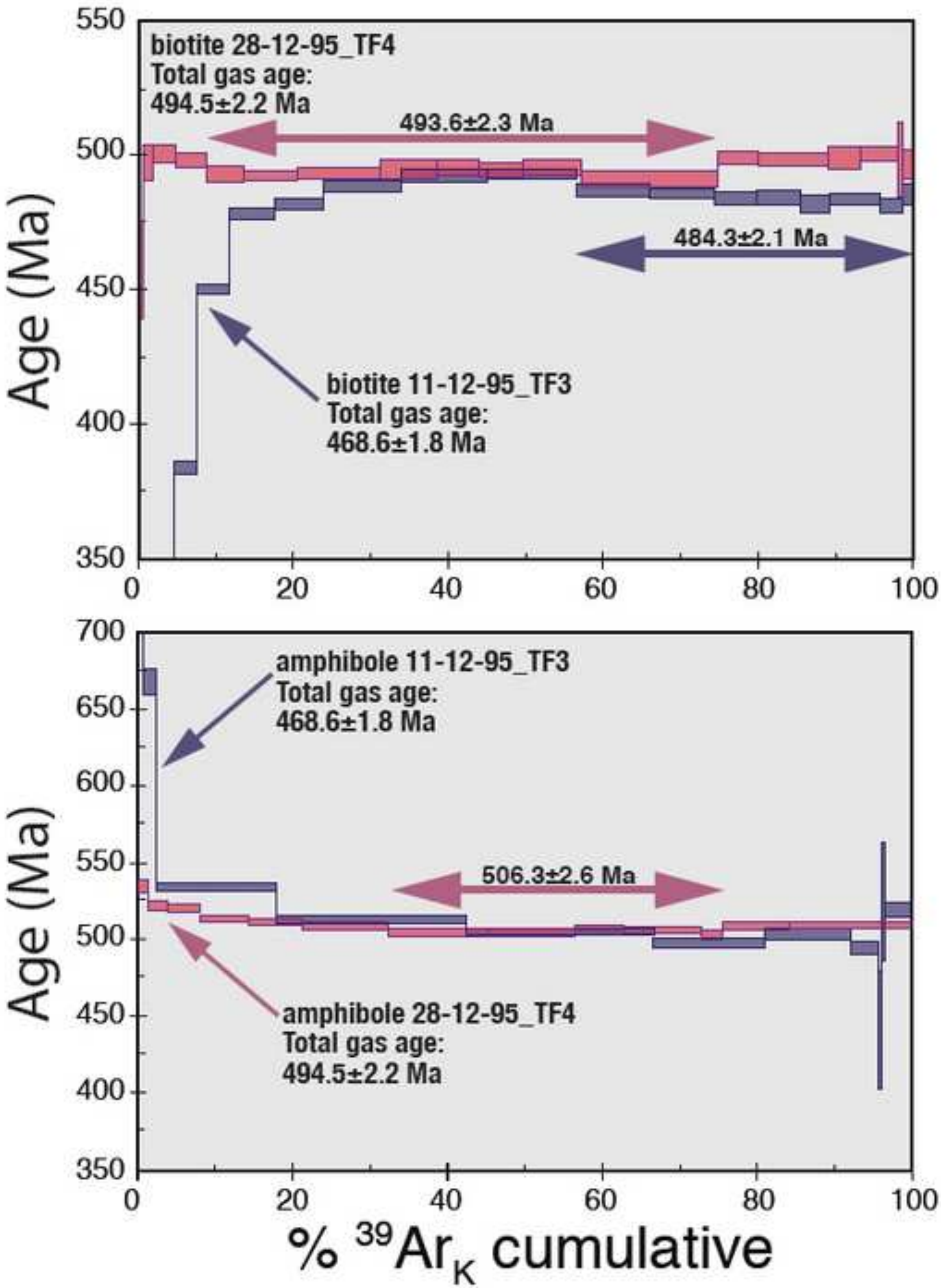

Figure 10

Click here to download high resolution image

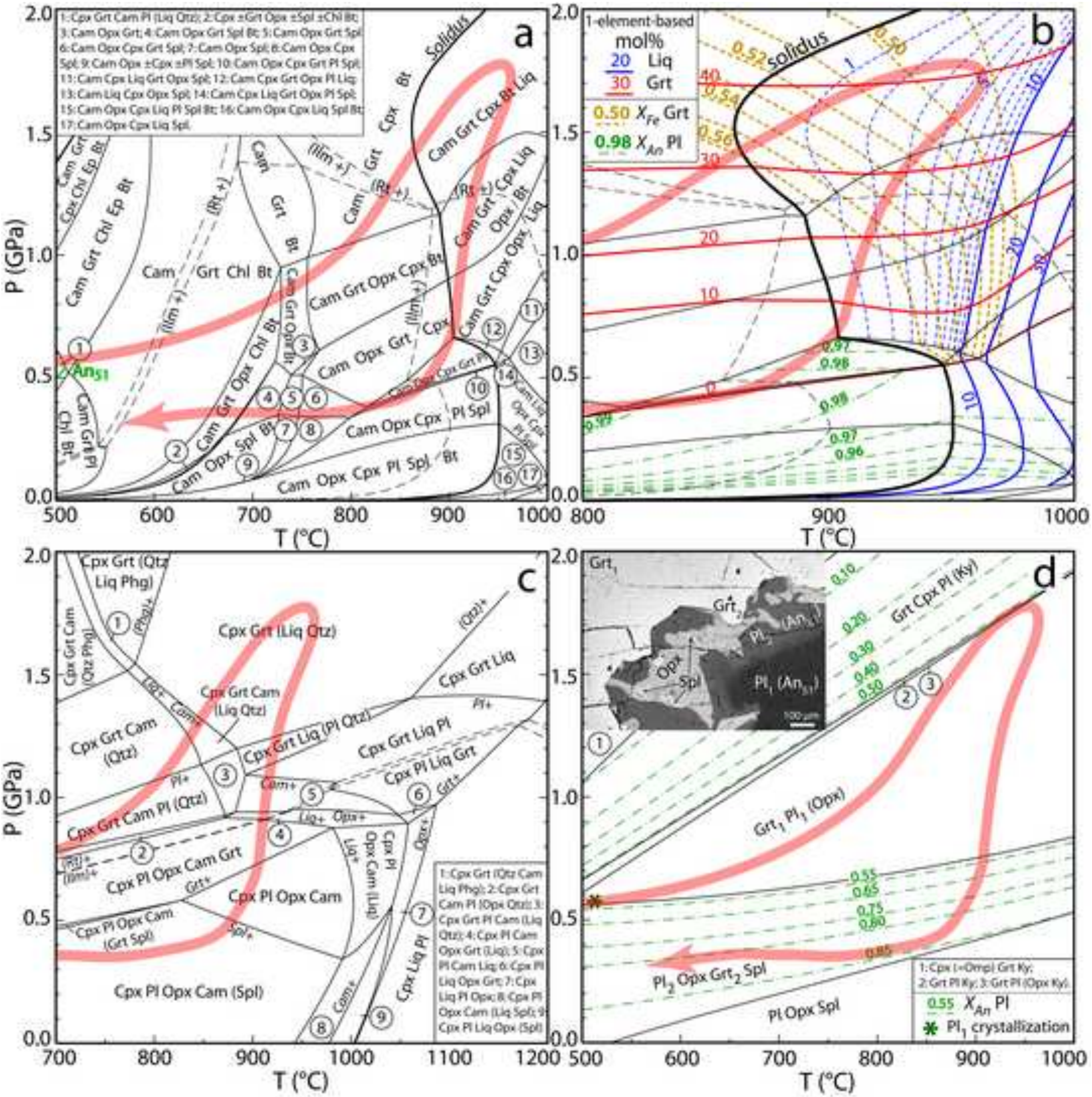

Figure 11

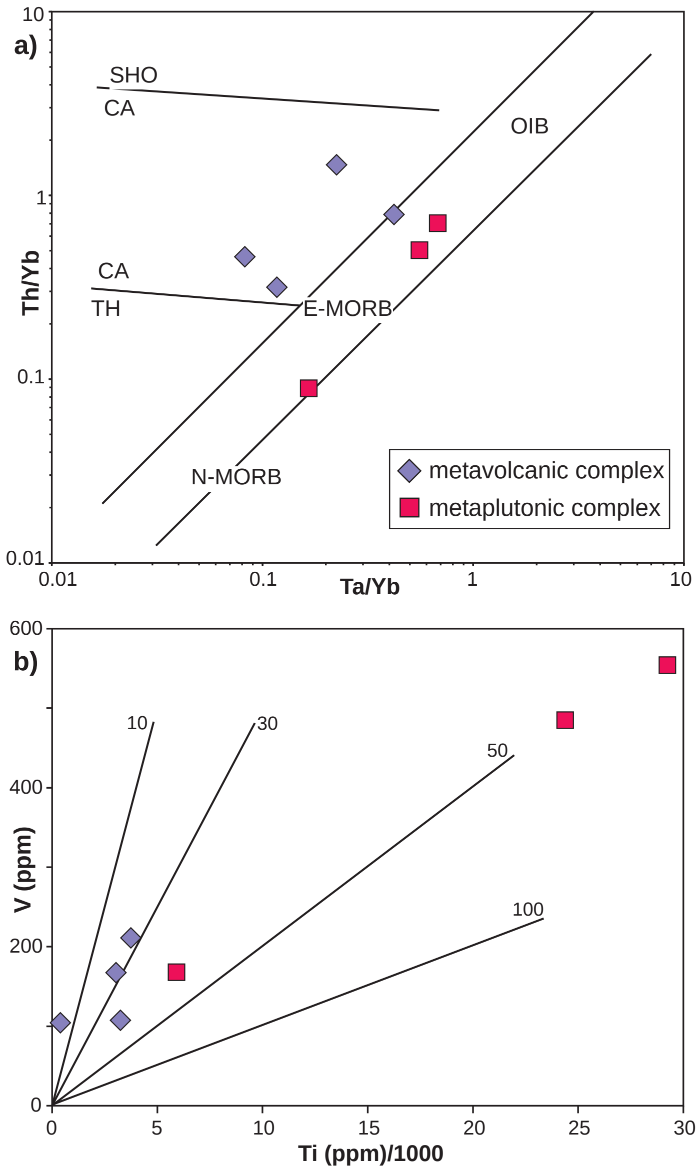
a)
SHO
CA
OIB
CA
TH
E-MORB
N-MORB
metavolcanic complex
metaplutonic complex
Th/Yb
Ta/Yb
10
1
0.1
0.01
0.01
0.1
1
10
b)
10
30
50
100
V (ppm)
Ti (ppm)/1000
600
400
200
0
0
5
10
15
20
25
30

Figure 12

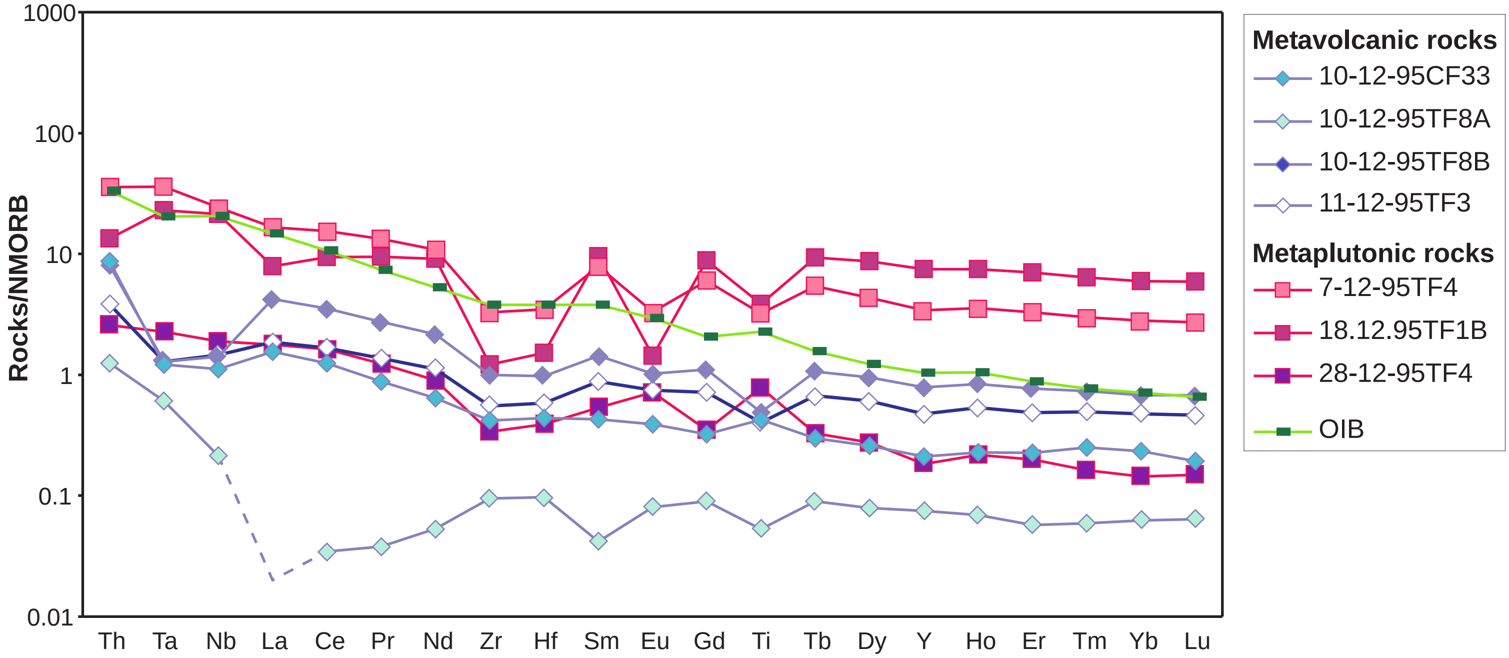
1000
100
10
1
0.1
0.01
Rocks/NMORB
Th Ta Nb La Ce Pr Nd Zr Hf Sm Eu Gd Ti Tb Dy Y Ho Er Tm Yb Lu
Metavolcanic rocks
10-12-95CF33
10-12-95TF8A
10-12-95TF8B
11-12-95TF3
Metaplutonic rocks
7-12-95TF4
18.12.95TF1B
28-12-95TF4
OIB

Figure 13

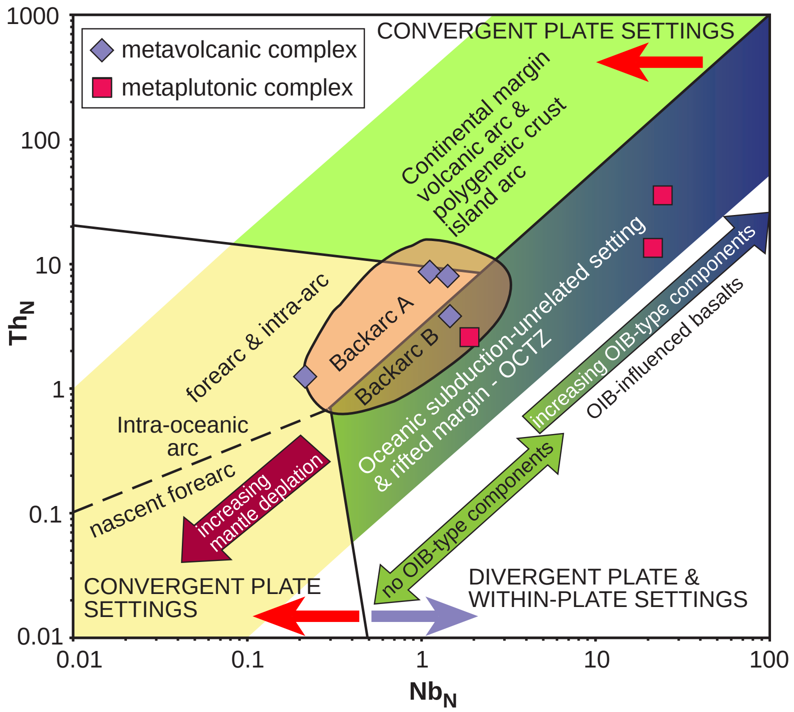

metavolcanic complex
metaplutonic complex
CONVERGENT PLATE SETTINGS
Continental margin volcanic arc & polygenetic crust island arc
forearc & intra-arc
Backarc A
Backarc B
Oceanic subduction-unrelated setting & rifted margin - OCTZ
increasing OIB-type components
OIB-influenced basalts
no OIB-type components
Intra-oceanic arc
nascent forearc
increasing mantle deplation
CONVERGENT PLATE SETTINGS
DIVERGENT PLATE & WITHIN-PLATE SETTINGS
1000
100
10
1
0.1
0.01
0.01
0.1
1
10
100
Th_N
Nb_N

Table 1

Click here to download Table: Palmeri et al_Table 1.xls

	Metavolcanic complex				Metaplutonic complex		
	10-12-95 CF33	11-12-95 TF3	10-12-95 TF8A	10-12-95 TF8B	7-12-95 TF4	18-12-95TF1B	28-12-95 TF4
Major elements (wt %)							
SiO_2	47.9	46.88	45.76	48.33	44.03	38.01	44.29
TiO_2	0.54	0.509	0.067	0.624	4.071	4.882	0.993
Al_2O_3	7.24	13.22	13.47	16.52	14.14	10.87	15.61
Fe_2O_{3t}	14.82	11.14	8.66	8.89	19.02	28.61	14.24
MnO	0.194	0.178	0.148	0.132	0.295	0.582	0.186
MgO	26.17	13.32	14.67	8.26	5.19	6.06	13.74
CaO	3.21	10.55	13.41	12.38	11.07	11.08	10.06
Na_2O	0.63	1.42	2.12	2.66	1.57	0.22	1.04
K_2O	0.2	1.81	0.32	0.95	0.77	0.05	0.87
P_2O_5	0.08	0.05	< 0.01	0.09	0.54	0.48	0.02
LOI	-0.35	1.64	1.32	0.44	-0.27	-0.79	-0.19
Total	100.6	100.7	99.96	99.27	100.4	100.1	100.9
#Mg	60.35	50.76	59.35	44.47	19.04	15.44	45.41
Trace elements (ppm)							
Ni	930	310	100	130	50	< 20	170
Cr	2440	280	270	100	80	30	130
Co	109	51	65	43	40	44	81
V	108	167	104	212	485	553	167
Sc	15	26	43	38	57	79	21
Cu	20	< 10	< 10	20	20	80	10
Zn	170	140	50	80	220	120	100
Ga	10	15	6	20	29	16	16
Pb	8	< 5	< 5	< 5	6	< 5	< 5
Sr	29	80	34	245	47	49	161
Rb	4	62	2	7	18	1	13
Ba	10	136	19	68	139	3	74
Zr	31	41	7	74	244	90	25
Hf	0.9	1.2	0.2	2	7.1	3.1	0.8
Nb	2.6	3.4	0.5	3.3	56.6	49.9	4.4
Ta	0.16	0.17	0.08	0.17	4.74	3.03	0.3
Th	1.04	0.46	0.15	0.96	4.27	1.61	0.31
U	0.79	0.54	0.06	0.61	4.08	0.46	0.13
Y	5.9	13.3	2.1	22	96	209	5.1
La	3.87	4.66	< 0.05	10.6	41.4	19.8	4.44
Ce	9.32	12.5	0.26	26.4	116	70.3	12.2
Pr	1.16	1.81	0.05	3.63	17.6	12.5	1.63
Nd	4.7	8.11	0.39	15.8	78.9	66.3	6.58
Sm	1.13	2.31	0.11	3.79	20.8	25.1	1.41
Eu	0.399	0.76	0.082	1.04	3.39	1.47	0.73
Gd	1.19	2.63	0.33	4.07	22.1	32.5	1.29
Tb	0.2	0.45	0.06	0.71	3.62	6.23	0.22
Dy	1.18	2.77	0.36	4.32	19.8	39.4	1.25
Ho	0.23	0.54	0.07	0.85	3.59	7.55	0.22
Er	0.67	1.44	0.17	2.28	9.75	20.8	0.59
Tm	0.114	0.226	0.027	0.334	1.36	2.91	0.074
Yb	0.71	1.45	0.19	2.07	8.54	18.2	0.44
Lu	0.088	0.211	0.029	0.308	1.24	2.68	0.068
Σ_{REE}	24.96	39.87	2.13	76.20	348.09	325.74	31.14
$(La/Sm)_N$	2.211	1.302	0.591[i]	1.806	1.285	0.509	2.033
$(Gd/Yb)_N$	1.387	1.500	1.437	1.627	2.141	1.477	2.425
Eu/Eu*	1.044	0.939	1.216	0.805	0.480	0.157	1.625

Table S1

Click here to download Supplementary Interactive Plot Data (CSV): Palmeri et al_Table S1.xls

Table S2
Click here to download Supplementary Interactive Plot Data (CSV): Palmeri et al_Table S2.xls

Table S3

Click here to download Supplementary Interactive Plot Data (CSV): Palmeri et al_Table S3.xls

Table S4

Click here to download Supplementary Interactive Plot Data (CSV): Palmeri et al_Table S4.xls

Table S5

Click here to download Supplementary Interactive Plot Data (CSV): Palmeri et al_Table S5.xls

Table S6

Click here to download Supplementary Interactive Plot Data (CSV): Palmeri et al_Table S6.xls

explanatory for supplementary material
Click here to download Supplementary Interactive Plot Data (CSV): Supplementary Material.docx

Fig.S1

Fig.S2